Boundary-Layer Meteorology (2020) 175:203–235
https://doi.org/10.1007/s10546-020-00502-3

RESEARCH ARTICLE

Coordinate Rotation–Amplification in the Uncertainty and Bias in Non-orthogonal Sonic Anemometer Vertical Wind Speeds

John M. Frank[1] · William J. Massman[1] · W. Stephen Chan[2] · Keith Nowicki[3] · Scot C. R. Rafkin[3]

Received: 12 April 2019 / Accepted: 23 January 2020 / Published online: 28 February 2020

Abstract
Recent research indicates that non-orthogonal sonic anemometers underestimate vertical wind velocity and consequently eddy-covariance fluxes of mass and energy. Whether this is a general problem among all non-orthogonal sonic anemometers, including those calibrated for flow-shadowing effects, is unknown. To investigate this, we test two sonic anemometer designs, orthogonal (3Vx-probe, Applied Technologies, Inc.) and non-orthogonal (R3-50, Gill Instruments, Ltd.), in a series of field manipulation experiments featuring replicate instruments mounted in various orientations, and use a Bayesian analysis to determine the most likely posterior correction to produce equivalent measurements. The 3Vx-probe experiment was conducted on a 24-m scaffold at the Glacier Lakes Ecosystem Experiments Site (GLEES), Wyoming, USA AmeriFlux site while R3-50 anemometer experiments were conducted at the GLEES field site and on a 2.9-m scaffold at the Pawnee National Grassland, Colorado, USA. Without applying a shadowing correction to the 3Vx-probe, the posterior correction significantly increases the standard deviation of the horizontal velocity component by 5–15% (95% Bayesian credible interval) but without a significant change in the horizontal temperature flux; with the shadowing correction applied neither of these have significant changes. Similarly, for the R3-50 GLEES experiment, the standard deviation of the vertical velocity and vertical temperature flux significantly increase by 13–18% and 6–10% (95% credible intervals); results from the Pawnee experiment are contradictory and inconclusive. The reason for the underestimated vertical velocity is undetermined, though a mathematical by-product of the non-orthogonal geometry is that small systematic measurement biases

Electronic supplementary material The online version of this article (https://doi.org/10.1007/s10546-020-00502-3) contains supplementary material, which is available to authorized users.

✉ John M. Frank
john.frank@usda.gov

1 Rocky Mountain Research Station, USDA Forest Service, 240 W. Prospect Rd., Fort Collins, CO 80526, USA

2 Lawrence Berkeley National Laboratory, 1 Cyclotron Rd., Berkeley, CA 94720, USA

3 Southwest Research Institute, 1050 Walnut St., Suite 300, Boulder, CO 80302, USA

can become large uncertainties in the vertical velocity. This could affect all non-orthogonal designs.

Keywords Bayesian statistics · Eddy covariance · Sonic anemometry

1 Introduction

The eddy-covariance technique is ubiquitous in micrometeorological and ecological studies of energy and mass exchange between the land surface and atmosphere. At the core of these flux measurements is the sonic anemometer, an instrument that rapidly measures the three-dimensional (3D) wind velocity components. Over the past decade, a consensus has been growing that some non-orthogonal sonic anemometers underestimate the vertical velocity component because of uncorrected flow shadowing. A diverse set of experiments identified a range of underestimates on several models from different manufacturers: R.M. Young 81000 (Kochendorfer et al. 2012, 2013; Mauder 2013), Campbell Scientific CSAT3 (Frank et al. 2013), and Gill WindMaster (Nakai and Shimoyama 2012). Horst et al. (2015) was the first to demonstrate a link between these underestimates to the lack of a transducer-shadowing correction in the CSAT3, which was later supported by Frank et al. (2016b). Frank et al. (2016a) provided evidence that structural shadowing and transducer cross-shadowing could roughly double this underestimate. Huq et al. (2017) performed a numerical simulation that exposed a CSAT3 to turbulent airflow and quantified the vertical velocity underestimation, of which roughly 60% corresponded to a theoretical transducer-shadowing algorithm (Kaimal 1979; Wyngaard and Zhang 1985). However, a field study using a Doppler lidar (Mauder et al. 2019) did not find these disparities. Meanwhile, the "*w*-boost" bug in the Gill WindMaster (Billesbach et al. 2019) clearly illustrates that other non-orthogonal anemometers have erroneous vertical velocity measurements. Recently, Mauder and Zeeman (2018) compared six non-orthogonal anemometers from four manufacturers and found minimal differences in the vertical velocity measurements. Because a CSAT3 was included in the intercomparison, they concluded that all of these anemometers could be "afflicted with an error of almost the exact same magnitude". Yet, when many of these non-orthogonal anemometers are compared to orthogonal anemometers, systematic differences in vertical velocity measurements are often observed between these two fundamentally different designs (Mauder et al. 2007; Kochendorfer et al. 2012; Frank et al. 2016b), though not all investigations have found these disparities (Loescher et al. 2005; Mauder 2013).

A recent field intercomparison between a non-orthogonal (model R3-50, Gill Instruments Ltd., Hampshire, UK) and an orthogonal anemometer (3Vx-probe, Applied Technologies Inc., henceforth ATI, Longmont, CO, USA) during an AmeriFlux site visit observed that the orthogonal anemometer measured 13% larger standard deviations of vertical velocity and 8% larger sensible heat fluxes (https://doi.org/10.2737/RDS-2019-0013). The results from that intercomparison indicate that the vertical velocity could be erroneous in either or both the Gill R3-50 and the ATI 3Vx-probe, which is surprising, considering both are manufacturer corrected for shadowing effects. In general, should the vertical velocity of the Gill R3-50 be in error, the consequences would be extensive considering it is the sonic anemometer featured in the AmeriFlux portable eddy covariance system (http://ameriflux.lbl.gov/portable-eddy-covariance-system/) which is a roving system that effectively serves as a secondary calibration standard for the AmeriFlux network. Therefore, our study investigates whether there is observational evidence of, or a plausible explanation for, vertical velocity errors in either the Gill R3-50 or the ATI 3Vx-probe.

Considering that Mauder and Zeeman (2018) tested the Gill-R3 against other non-orthogonal sonic anemometers and found that its vertical velocity measurements were similar, it would be unlikely that such an error could be attributed to a specific anemometer or manufacturer. Also, as most non-orthogonal anemometers are calibrated or corrected for shadowing effects, no obvious explanation exists for how different non-orthogonal anemometers could share a common cause for vertical velocity underestimates. Beyond the specific cases of the CSAT3 and the "*w*-boost" in the Gill WindMaster, there is little direct evidence to implicate a root cause for potential errors in other non-orthogonal anemometers. To better understand this, we investigate the consequences of the non-orthogonal transformation, which mathematically could lead to uncertainties and enhance systematic underestimates of the vertical velocity in all non-orthogonal sonic anemometers.

To investigate possible errors in the vertical velocity in either the Gill R3-50 or the ATI 3Vx-probe, we performed manipulation experiments on these non-orthogonal and orthogonal sonic anemometers and used Bayesian analyses to quantify posterior 3D corrections required to yield similar velocity measurements with differently mounted anemometers. We evaluate these hypotheses: (1) In a typical field deployment, transducer shadowing in an orthogonal anemometer causes sizeable underestimates in the horizontal velocity component that can be mitigated with a manufacturer recommended correction; (2) In a typical field deployment of a non-orthogonal anemometer that is factory calibrated to remove the effect of the transducers and supporting structure, the vertical velocity can be underestimated; (3) A mathematical byproduct of the non-orthogonal geometry is that small transducer measurement biases can be transformed into large systematic uncertainties in the vertical velocity within a wide range of flow inclinations (i.e., angles of attack). Consequently, a large proportion of the global ground-based measurements of trace gas concentrations (i.e., carbon dioxide, water vapour, methane) and energy fluxes could likewise be underestimated, leading to many implications for studies and models that use these data to investigate ecohydrological processes and their effect on the global climate.

2 Methods

2.1 Orthogonal Anemometer Experiment Over a Subalpine Forest

We tested hypothesis (1) with a manipulation experiment where two replicate orthogonal sonic anemometers were deployed atop of a scaffold with one mounted vertically and the other horizontally. The ATI 3Vx-probe anemometer has transducers aligned to measure wind velocity components in orthogonal sonic anemometer coordinates (u_s, v_s, and w_s). The u_s and v_s transducers are located 45° from the instrument boom on a supporting structure that is a 270° arc confined to the horizontal plane; the supporting structure for the two w_s transducers is a 180° arc confined to the vertical plane aligned with the instrument boom (Fig. 1). The transducers have a diameter $d = 0.0096$ m and are spaced a distance $L = 0.143$ m apart ($L/d \approx 15$). The manufacturer recommends a transducer-shadowing correction based on the wind direction and angle of attack described by Kaimal (1979) and Kaimal et al. (1990), which is defined for any of the three dimensions (i.e., $x = u$, v, or w) and the angle between the flow and the transducer axis, θ, as $x_s = (0.84 - 0.16\theta/70)\ \hat{x}_s$ for $\theta \leq 70°$ and $x_s = \hat{x}_s$ for

Fig. 1 The ATI 3Vx-probe GLEES experiment. The anemometer on the left is horizontally rotated around the u_c axis

$\theta > 70°$ where x_s is the original measurement and $\hat{x}_s$ is the corrected measurement; all data were collected without this correction applied.

The anemometers were deployed atop of the Glacier Lakes Ecosystem Experiments Site (GLEES) AmeriFlux scaffold (US-GLE, ameriflux.lbl.gov) at a height of 24 m, mounted on booms pointed due west extending 2 m from the scaffold, and with 0.70-m lateral separation from each other. The GLEES field site is in the Snowy Range mountains of south-eastern Wyoming, USA and is a high elevation subalpine Engelmann spruce (*Picea engelmannii*)–subalpine fir (*Abies lasiocarpa*) forest with a canopy that reaches 18 m, and average canopy height of 7 m, and with much of the overstorey recently denuded of needles from a recent spruce beetle (*Dendroctonous rufipennis*) outbreak. The scaffold is located at 41.3665° N and 106.2400° W at 3190 m elevation above sea level (a.s.l.). The AmeriFlux site is described by Frank et al. (2014). We defined orthogonal cardinal coordinates such that u_c is east, v_c is north, and w_c is upward. The instruments, serial numbers 121101 and 121102, were customized by Applied Technologies Inc. to report only the time of flight between sonic transducers such that calculations of velocity were performed in post-processing of the dataset (Nowicki in prep). Applied Technologies Inc. sonic anemometers typically measure at 200 Hz and are often downsampled to lower frequencies by averaging or selecting the median of a group of these higher frequency measurements; for the custom anemometers only outgoing/incoming time of flight measurement pairs that occurred at 20 Hz were recorded (i.e., no averaging or median selecting between consecutive measurements, etc.) leading directly to the post-processed 20-Hz velocity signals. Otherwise, their mechanical and electronic construction was identical to the standard ATI 3Vx-probe. The instruments were installed on 28 July 2016 with both mounted vertically so that their u_s axes were pointed 135° to the south-east, their v_s axes were north-east at 45°, and their w_s axes were pointed upward. The data during this time were used to evaluate a fibre-optic laser hygrometer and is not reported here. The first manipulation was performed on 15 September 2016 when the northern anemometer was rotated 90° around its boom (i.e., u_c axis) such that its w_s axis was in the horizontal plane pointing southward and the other axes were vertically aligned with the boom with u_s pointed 45° downward and v_s pointed 45° upward. The second manipulation was performed on 20 September 2016, when the southern anemometer was likewise rotated 90° around its boom and the northern anemometer was returned to the vertical position (Fig. 1). The instruments were removed on 29 September 2016. A supplemental deployment was conducted from 18 December 2018 to 1 January 2019 to collect data with the two anemometers vertically mounted. All data were collected using LabView (Version 12.0, National Instruments). For all experiments, the data were screened for quality control (Vickers and Mahrt 1997) with questionable 5-min periods removed. At the GLEES field site, most instantaneous wind directions are between 225° and 335° (Frank et al. 2016b), thus it was anticipated that a minimal amount of data would experience cross-wind flow distortions between the anemometers. Therefore, for all GLEES experiments, all fast-response data were included in the subsequent analyses, regardless of wind direction.

2.2 Non-orthogonal Anemometer Experiment Over a Subalpine Forest

We evaluated hypothesis (2) with an experiment testing three non-orthogonal sonic anemometers (Gill R3-50) atop of the GLEES scaffold conducted from 7 February to 14 March 2017 (Fig. 2). The Gill R3-50 is a non-orthogonal anemometer where three transducer pairs stem from central hubs located above and below the measurement volume, which are themselves supported by spars that form a cage around the instrument. When viewed from the side, the

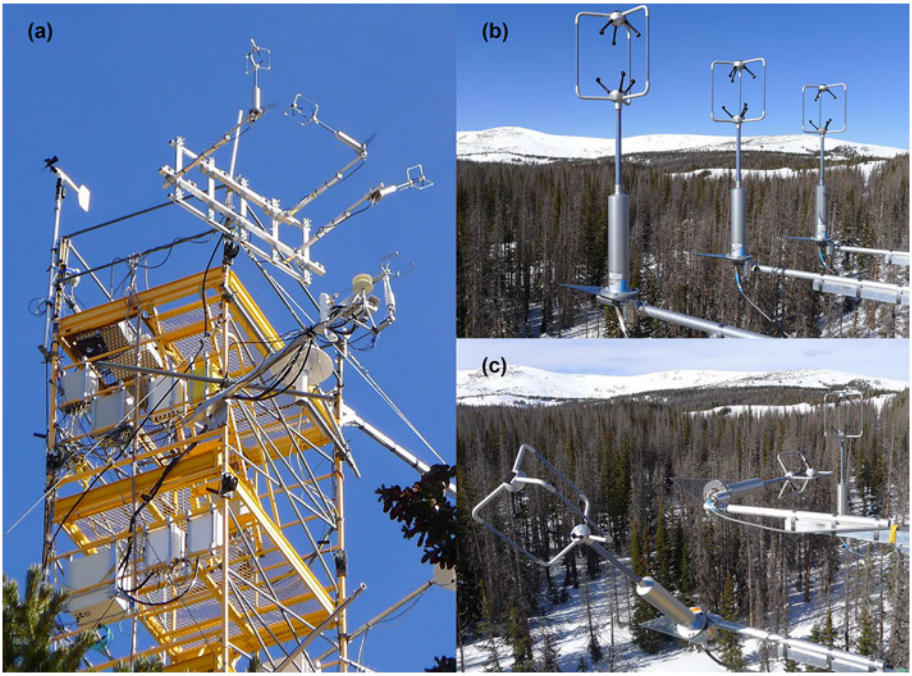

Fig. 2 The Gill R3-50 experiment (**a**) on top of the GLEES AmeriFlux scaffold. All anemometers were (**b**) vertically mounted, and then (**c**) manipulated to horizontal and a 45° tilt around the u_c axis

transducers are tilted 45° from vertical. When viewed from above the transducers are 120° apart, the supporting spars are 120° apart, and the transducers are separated from the supporting spars by 30°. The instrument performs a matrix transformation to produce the velocity in orthogonal sonic coordinates where the u_s measurement is aligned with a supporting spar demarcated as "N" and with the v_s axis separated by 30° from the other two supporting spars. The transducers have a diameter that tapers between $d = 0.0105$ m and 0.0115 m and are spaced a distance $L = 0.1466$ m apart ($L/d \approx 13$–14). A brief summary of the Gill R3-50 calibration is as follows. First, raw voltages are amplified to produce velocities with a positive adjustment factor resulting in values that are generally similar across all R3-50 instruments. Second, each anemometer is individually calibrated in a UKAS-accredited wind tunnel under laminar flow at 12 m s^{-1} where the instrument is vertically mounted and rotated from 0° to 360° at increments of 1°; subsequent checks are performed at 32 m s^{-1}. A proprietary software tool is used to perform this calibration and the results are written into the firmware. Though this step focuses on horizontal measurements, the w component is adjusted based on the adjustments to u and v. Third, an empirically derived look-up table specific to the R3/R3-50 products is used to apply angle of attack corrections. Though the details are proprietary, the correction is asymmetric, dependent on wind inclination and the mechanical structure apparent at that inclination, and, to a degree, is meant to correct for transducer shadowing and flow distortion.

The three anemometers in this experiment are the same as used in the AmeriFlux portable eddy covariance system (serial numbers 549, 550, and 572, henceforth #1, #2, and #3). The anemometers were mounted on separate booms pointed due west (i.e., along the u_c axis) which served as the axes of rotation for each experimental manipulation. The vertically-mounted anemometers were affixed to their booms with their "N" demarcations aimed at 330°, which aligned the support spars symmetrically along the vertical east–west plane. For vertical anemometers, u_s and v_s were in the horizontal plane at 330° and 240°, respectively, while w_s was pointed up; for horizontal anemometers, u_s was aligned west pointing down at 60°, v_s was aligned west pointing up at 30°, and w_s in the horizontal plane at 0°. A third orientation was included in the experiment where the anemometer was tilted 45° south around the boom (i.e., u_c axis). All anemometers were initially mounted upright, laterally from south to north (ordered as #2, #1, and #3), with 0.70 m separation, with their centres at 24.3 m above the ground (Fig. 2b). The first manipulation on 14 February rotated the southmost anemometer (position 1) to tilted, the middle anemometer (position 2) to horizontal, and the northmost (position 3) was unchanged (Fig. 2c). In this arrangement the lateral separation between the anemometers was 1.32 m between positions 1 and 2 (from tilted to horizontally mounted) and 0.50 m between positions 2 and 3 (from horizontally to vertically mounted); the vertical separation was − 0.07 m between position 1 and 2 and 0.24 m between position 2 and 3. In the second manipulation on 21 February, the anemometers were reordered from south to north as #1, #3, and #2, with the locations of each rotation remaining the same. A final manipulation was performed on 3 March when the anemometers were reordered as #3, #2, and #1. The angle of each rotation was verified to within ± 0.3° with a digital clinometer. All data were synchronized and collected at 10 Hz via serial communications (RS-422) by a computer using Huskerflux software (https://github.com/Flux-Dave/HuskerFlux).

2.3 Non-orthogonal Anemometer Experiment Over a Short-Grass Prairie

The non-orthogonal experiment was repeated over a short-grass prairie site at the Pawnee National Grassland, Colorado, USA (40.8119° N, 104.0391° W, 1665 m a.s.l.) from 22 March to 3 April 2017 (Fig. 1 in the supplementary material). The study area was perched atop a relatively flat bluff with short vegetation cover (<0.1 m near the equipment) comprised of grasses, prickly pear cactus, and yucca. The area within a 120-m radius of the anemometers was flat, with the edge of the escarpment about 120 m to the east, 160 m to the south, and 600 m to the west, and with a draw forming about 150 m to the north. The experiment used the same cardinal coordinate system (i.e., booms aimed west, u_c east, v_c north, w_c up). The centres of the anemometers were 2.94 m above the ground and 0.69 m west of one section of scaffold of the same style as at the GLEES field site. All anemometers were initially mounted upright, laterally from south to north (ordered as #2, #3, #1), and with 1.02 m separation (Fig. 1b in the supplementary material). The first manipulation on 24 March rotated the southmost anemometer (position 1) to tilted, the middle anemometer (position 2) was unchanged, and the northmost (position 3) to horizontal (Fig. 1c in the supplementary material). The separation between anemometer centres did not change. A second manipulation was performed on 30 March when the anemometers were reordered from south to north as #3, #1, and #2, with the locations of each rotation remaining the same. In a final manipulation on 2 April the anemometers were reordered as #1, #2, and #3. The angle of each rotation was verified to within $\pm 0.3°$. Similar to the GLEES experiments, all fast-response data at the Pawnee National Grassland were included in the subsequent analysis, regardless of their wind direction.

2.4 Statistical Analyses

Similar to Frank et al. (2016a), the data were analyzed with Bayesian statistics using the Markov chain Monte Carlo (MCMC) method, Gibbs sampling, and the Metropolis–Hastings algorithm (Kruschke 2014). The basic approach is summarized as follows. The 3D space around the anemometer is divided into approximately equally spaced grid points, the nearest of which is assigned to each fast-response velocity measurement. A 3D correction is created and initialized to a prior value for each of the grid points. For each step in the MCMC chain, a new correction is proposed for a grid point. The new correction is applied to the fast-response dataset, which is then summarized into 5-min standard deviations along the cardinal dimensions (σ_{u_c}, σ_{v_c}, and σ_{w_c}). The probability that all anemometers are more similar with the new correction compared to the old correction (i.e., the Metropolis–Hastings ratio) is used to either retain or reject the proposed correction. Each MCMC step proceeds until the correction for all grid points is updated. Once that is done the entire process is repeated with a new MCMC step, and so forth. After sufficient burn in, the 3D correction becomes a posterior distribution. Like Frank et al. (2016a), we used symmetry to reduce the number of unique statistical process parameters required to define the correction for all grid points around the three transducer pairs. For the ATI 3Vx-probe, the 3D grid was divided into 522 points. The u_s and v_s transducer axes each have top/bottom symmetry and are mirror images of each other such that they could be characterized with 281 unique parameters; the w_s correction was calculated separately and required 147 unique parameters due to top/bottom and right/left symmetry. The 3D grid for the Gill R3-50 was divided into 512 points, which assumed the three transducer axes were top/bottom symmetrical and 120° rotations of each other to reduce the number of required unique parameters to 256.

Except for the following changes, a detailed description of the Bayesian model and an Appendix deriving the univariate conditional posterior distribution functions are found in

Frank et al. (2016a). The matrix transformation that converts the Gill R3-50 from non-orthogonal transducer coordinates (u_1, u_2, and u_3) to orthogonal sonic coordinates is

$$\begin{bmatrix} u_s \\ v_s \\ w_s \end{bmatrix} = \begin{bmatrix} \frac{\sqrt{2}}{\sqrt{3}} & 0 & -\frac{\sqrt{2}}{\sqrt{3}} \\ \frac{\sqrt{2}}{3} & -\frac{2\sqrt{2}}{3} & \frac{\sqrt{2}}{3} \\ \frac{\sqrt{2}}{3} & \frac{\sqrt{2}}{3} & \frac{\sqrt{2}}{3} \end{bmatrix} \begin{bmatrix} u_1 \\ u_2 \\ u_3 \end{bmatrix} \tag{1}$$

Equation 1 is solved for velocities in non-orthogonal transducer coordinates by inversion,

$$\begin{bmatrix} u_1 \\ u_2 \\ u_3 \end{bmatrix} = \begin{bmatrix} \frac{\sqrt{3}}{2\sqrt{2}} & \frac{1}{2\sqrt{2}} & \frac{1}{\sqrt{2}} \\ 0 & -\frac{1}{\sqrt{2}} & \frac{1}{\sqrt{2}} \\ -\frac{\sqrt{3}}{2\sqrt{2}} & \frac{1}{2\sqrt{2}} & \frac{1}{\sqrt{2}} \end{bmatrix} \begin{bmatrix} u_s \\ v_s \\ w_s \end{bmatrix}. \tag{2}$$

The matrices that convert the Gill R3-50 GLEES experiment from orthogonal sonic coordinates to cardinal coordinates are

$$\begin{bmatrix} u_c \\ v_c \\ w_c \end{bmatrix} = \begin{cases} \begin{bmatrix} -\frac{1}{2} & -\frac{\sqrt{3}}{2} & 0 \\ \frac{\sqrt{3}}{2} & -\frac{1}{2} & 0 \\ 0 & 0 & 1 \end{bmatrix} \begin{bmatrix} u_s \\ v_s \\ w_s \end{bmatrix} \text{vertical} \\ \begin{bmatrix} -\frac{1}{2} & -\frac{\sqrt{3}}{2} & 0 \\ 0 & 0 & 1 \\ -\frac{\sqrt{3}}{2} & \frac{1}{2} & 0 \end{bmatrix} \begin{bmatrix} u_s \\ v_s \\ w_s \end{bmatrix} \text{horizontal} \\ \begin{bmatrix} -\frac{1}{2} & -\frac{\sqrt{3}}{2} & 0 \\ \frac{\sqrt{3}}{2\sqrt{2}} & -\frac{1}{2\sqrt{2}} & -\frac{1}{\sqrt{2}} \\ \frac{\sqrt{3}}{2\sqrt{2}} & -\frac{1}{2\sqrt{2}} & \frac{1}{\sqrt{2}} \end{bmatrix} \begin{bmatrix} u_s \\ v_s \\ w_s \end{bmatrix} \text{tilted} \end{cases} \tag{3}$$

During the Pawnee experiment, the matrix for the horizontal mounting is slightly different, with opposite signs for the second and third rows. The matrices that convert the ATI 3Vx-probe GLEES experiment from orthogonal sonic coordinates to cardinal coordinates are

$$\begin{bmatrix} u_c \\ v_c \\ w_c \end{bmatrix} = \begin{cases} \begin{bmatrix} \frac{1}{\sqrt{2}} & \frac{1}{\sqrt{2}} & 0 \\ -\frac{1}{\sqrt{2}} & \frac{1}{\sqrt{2}} & 0 \\ 0 & 0 & 1 \end{bmatrix} \begin{bmatrix} u_s \\ v_s \\ w_s \end{bmatrix} \text{vertical} \\ \begin{bmatrix} \frac{1}{\sqrt{2}} & \frac{1}{\sqrt{2}} & 0 \\ 0 & 0 & -1 \\ -\frac{1}{\sqrt{2}} & \frac{1}{\sqrt{2}} & 0 \end{bmatrix} \begin{bmatrix} u_s \\ v_s \\ w_s \end{bmatrix} \text{horizontal} \end{cases} \tag{4}$$

Another difference in our study is that σ_{w_c} is weighted more than σ_{u_c} and σ_{v_c} in the Bayesian likelihood function. This was justified heuristically as we recognized that the results were sensitive to weighting the w measurement; i.e., corrected values were less noisy and the ratio between horizontal and vertical corrections became more stable. We beta tested a range of w weightings, and determined that the optimal coincided approximately with the ratio of $\sigma_{\sqrt{u_c^2+v_c^2}}$ to σ_{w_c}, i.e., the ratio of standard deviation of horizontal wind speed to standard deviation of vertical velocity. For the two GLEES experiments this meant w was weighted in the likelihood calculation by a factor of 1.5 while at the Pawnee site it was

2.25. Finally, we used embarrassingly-parallel MCMC techniques with high-performance computing (Rosenthal 2000; Wilkinson 2006; Neiswanger et al. 2014) to analyze the entire dataset from each experiment, unlike Frank et al. (2016a) who could only accommodate 5% of their original dataset. This was accomplished by performing numerous independent Bayesian analyses, each utilizing their own computer core, each beginning with different random number seeds, and collecting the posterior results from all analyses into a combined posterior distribution.

We performed all statistical analyses using the R software environment (R Core Team 2015) with a custom MCMC sampler using high performance computing provided by the University of Wyoming (Advanced Research Computing Center 2012). Each Bayesian analysis was composed of 100 embarrassingly-parallel analyses with each one including 1000 MCMC steps (burn-in was estimated to be completed within 200–300 steps). The posterior values from the final step of each parallel analysis were combined into overall posterior distributions. Similar to Frank et al. (2016a), each analysis required prior probability distributions for all statistical process parameters: the 428 parameters for the ATI 3Vx-probe and 256 for the Gill R3-50 that define the 3D correction for each grid point (normal distributions with mean $= 1$, i.e., a flat prior, and standard deviation $= 0.1$, i.e., $\pm 10\%$ uncertainty), the reference condition representing the "true" standard deviation of the 3D velocity components for each 5-min time period (uniform distributions), and the standard deviation of the normal distributions that model σ_{u_c}, σ_{v_c}, and σ_{w_c} (gamma distribution, defined in Frank et al. 2016a). The posterior 3D corrections obtained directly from the MCMC chains can only be interpreted in a relative sense, thus, similar to Frank et al. (2016a), we normalized each of the parallel MCMC results post hoc. To accomplish this, we make the assumptions that the posterior corrections should not change the average horizontal wind speed of an upright Gill R3-50 or the vertical velocities of an upright ATI 3Vx-probe. This does not mean that individual 5-min summary statistics cannot change, but rather, the averages of all 5-min values throughout the experiments cannot change. The normalization factor is determined from linear regression without intercept as the slope between $\sigma_{\sqrt{u_c^2+v_c^2}}$ or σ_{w_c} calculated without and with the final MCMC correction applied to the vertically-mounted anemometers. As discussed in Frank et al. (2016a), it is somewhat arbitrary to normalize the analyses to force particular measurements to be unchanged. For the Gill R3-50, choosing the horizontal wind speed to be unchanged is probably justified, considering the manufacturer specifically calibrates the horizontal velocity components across all 360° in an accredited wind tunnel. As the majority of eddies at the GLEES field site have small angles of attack (Frank et al. 2016b), it is assumed for at least the GLEES experiment the horizontal velocity calibration is reasonably accurate. Furthermore, Gill R3-50 horizontal velocity measurements have been shown to be accurate when compared to other objective standards in both wind tunnels and field environments (Grare et al. 2016). The justification in choosing the ATI 3Vx-probe vertical velocity measurement is based, in part, on the known inaccuracies in the u_s and v_s measurements. As demonstrated by Kaimal et al. (1990), the horizontal velocity components require a considerable amount of correction to be accurate. Conversely, Frank et al. (2016b) demonstrated that, based on current knowledge of transducer shadowing, w_s measurements require substantially less correction during a typical field deployment. While ejection events can cause air parcels to have more vertical than horizontal velocity, the vast majority of eddies at the GLEES field site do not fit this description, rather, they have angles of attack between $\pm 20°$ (Frank et al. 2016b) and their vertical velocity measurements are unchanged by the ATI shadowing-correction algorithm. While Frank et al. (2016b) also found evidence that uncorrected shadowing from the support structure might affect the vertical velocity measurement in an ATI K-probe, it is equally probable that the u_s and v_s measurements would have similar problems, especially with the Vx-probe which has a large support ring in the horizontal plane. As these potential problems remain mostly unquantified, based on current understanding of the instrument and the distribution of wind directions and angles of attack expected during the field deployments, the ATI vertical velocity is probably a more accurate measurement. We determine the relative change in measurements by performing a linear regression without intercept for each of the 100 parallel MCMC chains between values determined without and with the posterior 3D correction applied to vertical anemometers, and then combine various regression results to form a posterior distribution. The distribution of these regression slopes can be considered a derived quantity, which is a variable that is calculated from posterior parameters and thus has its own posterior probability distributions from which statistical inferences can be made (Hobbs and Hooten 2015). We make statistical inferences between posterior probability distributions by comparing their 95% credible intervals (Lu et al. 2012). We calculate the 5-min covariances between the 3D velocity components and the sonic anemometer virtual temperature and make similar assumptions of scaling post hoc: i.e., there should be no change in the average horizontal temperature covariance, $\overline{\left(\sqrt{u_c^2 + v_c^2}\right)' T'}$, of an upright Gill R3-50 or the vertical temperature covariance, $\overline{w_c' T'}$, of an upright ATI 3Vx-probe. Instead of making further modifications to the posterior 3D correction, we evaluate these derived quantities by dividing the regression slopes of the different covariances by the regression slope of either $\overline{\left(\sqrt{u_c^2 + v_c^2}\right)' T'}$ or $\overline{w_c' T'}$. To visibly enhance the differences between mountings or in applying the posterior corrections, we display all relationships as percent relative differences and present the median and root-median-square (r.m.s.) values. The r.m.s. is calculated from the residual differences, i.e., after the median has been removed. In order to appear similar, we report all regression slope results as their percent change from unity, i.e., slopes of 0.95, 1.00, and 1.05 are reported as − 5%, 0%, and 5%, respectively.

3 Results

3.1 Orthogonal Anemometer Experiment Over a Subalpine Forest

During the experiment, 1394 5-min periods of data were collected during the first manipulation (4.8 days) and 1569 were collected during the second manipulation (5.4 days). In the supplemental deployment, 2157 5-min periods of data were collected with both anemometers vertically mounted (7.5 days). Each 5-min period contained 6000 u_s, v_s, w_s, and sonic virtual temperature measurements from two anemometers. In all, the Bayesian analyses evaluated 106,704,000 unique measurements. The number of 20-Hz measurements available for each of the 522 grid points ranged from 13,361 to 2,663,924 (Fig. 2 in the supplementary material). Though no wind directions were excluded from the analysis, typical airflows were almost exclusively along the axis of the booms and almost never cross-wind between the anemometers (Fig. 2 in the supplementary material). Differences in momentum fluxes of vertically-mounted anemometers were used to check for potential flow distortions due to the scaffolding: the regression slope of $\overline{u'w'}$ (i.e., proportional to momentum flux) between the two anemometers was 3% different from unity while the friction velocity (u_*) differed by 2% (note, this analysis was conducted with the Kaimal shadowing correction applied).

The ATI 3Vx-probe without the Kaimal shadowing correction exhibited large measurement biases between differently mounted anemometers. Before the Bayesian analysis was

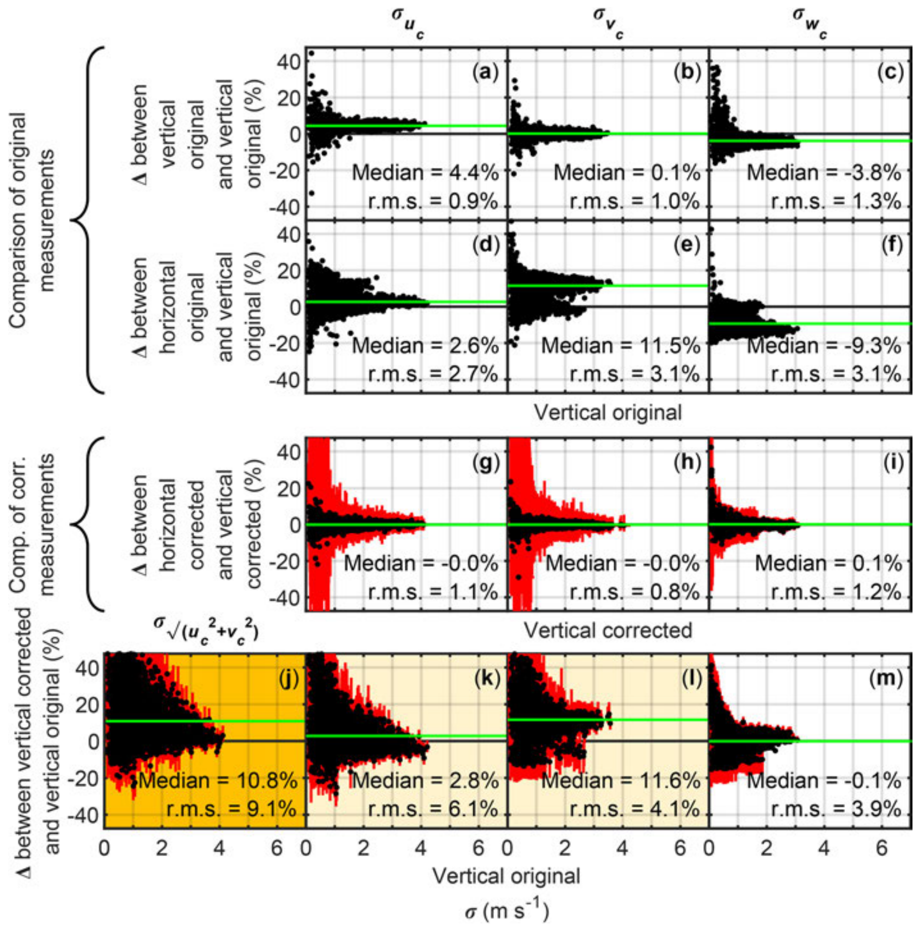

Fig. 3 Results from the ATI 3Vx-probe GLEES experiment without the Kaimal shadowing correction comparing σ, the 5-min standard deviation of wind velocity, for vertical and horizontal anemometers. u_C, v_C and w_C are velocity components in cardinal coordinates (i.e., east, north, up) and $\sqrt{(u_C^2 + v_C^2)}$ is the horizontal speed. **a**–**f** Comparison of original u_C, v_C, and w_C measurements between **a**–**c** vertical anemometers and **d**–**f** horizontal and vertical anemometers. **g**–**i** Comparison of u_C, v_C, and w_C measurements after applying the Bayesian posterior 3D correction between horizontal and vertical anemometers. **j**–**m** Comparison of original and corrected $\sqrt{(u_C^2 + v_C^2)}$, u_C, v_C, and w_C measurements for vertical anemometers. Results are presented as Δ, the percent relative difference between measurements. The median difference is listed and plotted in green. The root-median-square (r.m.s.) of the residual difference is listed. The 95% Bayesian credible intervals are presented in red

conducted, horizontally-mounted anemometers measured 11.5% larger σ_{v_C} and 9.3% smaller σ_{w_C} than those mounted vertically (Fig. 3e–f). After the Bayesian posterior 3D correction was applied to the 20-Hz time series data, the biases between differently mounted anemometers were effectively removed (medians in Fig. 3d–f vs. g–i). The posterior correction reduced the r.m.s. differences between vertical and horizontal instruments from 2.7–3.1 to 0.8–1.2% (Fig. 3d–f vs. g–i), which are comparable to the baseline r.m.s. differences between vertically-mounted anemometers (0.9–1.3%, Fig. 3a–c). When the posterior correction was applied to vertically-mounted anemometers, there was a significant increase in σ_{v_C} (11.6% median difference in Fig. 3l or alternatively 10% increase in the regression slope with 8–13% credible interval, credible interval, in Table 1) linked to a 12% increase in the covariance $\overline{v_c' T'}$ (12% increase in the regression slope with 8–16% credible interval in Table 1). The increase in σ_{v_c} led to a significant increase in $\sigma_{\sqrt{u_c^2+v_c^2}}$ (10.8% median difference in Fig. 3j or alternatively 9% increase in the regression slope with 5–15% credible interval in Table 1), though the covariance $\overline{\left(\sqrt{u_c^2+v_c^2}\right)' T'}$ did not change significantly (Table 1). Had the posterior correction been scaled using a different assumption (i.e., if the horizontal velocity was considered more accurate), then there would have been significant decreases in σ_{u_c} and $\overline{u_c' T'}$, a significant increase in $\overline{v_c' T'}$, and a significant decrease in σ_{w_c}.

In contrast, the ATI 3Vx-probe with the Kaimal shadowing correction was minimally biased between differently mounted anemometers. The only substantial difference was a 3.2% bias in σ_{v_c} (Fig. 4e) which was removed after applying the Bayesian posterior 3D correction to the 20-Hz time series data (medians in Fig. 4e vs. h). When the posterior correction was applied to vertically-mounted anemometers, there was a significant change in σ_{u_c} (− 2.6% median difference in Fig. 4k, or alternatively a − 4% change in the regression slope with − 6 to − 1% credible interval in Table 1), which was linked to a significant change in the covariance $\overline{u_c' T'}$ (− 5% change in the regression slope with − 10 to − 1% credible interval in Table 1). While there was an apparent increase in $\sigma_{\sqrt{u^2+v^2}}$ in Fig. 4j (3.4% median difference) this was neither a significant change in the regression slope (Table 1) nor was it linked to a significant change in the covariance $\overline{\left(\sqrt{u_c^2+v_c^2}\right)' T'}$ (Table 1). Had the posterior correction been scaled using the assumption that horizontal velocity was considered more accurate, then there would have been significant decreases in σ_{u_c} and $\overline{u_c' T'}$, a significant increase in $\overline{v_c' T'}$, though there would not be a significant change in σ_{w_c} or $\overline{w_c' T'}$.

The Bayesian posterior 3D corrections for the ATI 3Vx-probe appear similar, regardless of whether or not the Kaimal shadowing correction was included (Figs. 5a–f and 6). In each case, there is a region of intense correction roughly corresponding to direction of the boom and visually similar to a "+" (Fig. 6) which obscures the underlying transducer shadowing near one of the u_s transducers (at $\lambda = \pm 180°$, $\varphi = 0°$ in Fig. 6a) and one of the v_s transducers (at $\lambda = -90°$, $\varphi = 0°$ in Fig. 6c). While the location of this intense correction corresponds to the open end of the anemometer (i.e., right side of Fig. 5c,f) it also coincides with wind directions and angles of attack experienced by the anemometers during the experiment and the amount of data pooled for each grid location (Fig. 2 in the supplementary material). Transducer shadowing can be observed near one of the u_s transducers (at $\lambda = 0°$, $\varphi = 0°$ in Fig. 6a), one of the v_s transducers (at $\lambda = 90°$, $\varphi = 0°$ in Fig. 6c), and both of the w_s transducers (at $\varphi = \pm 90°$ in Fig. 6e). Less recognizable is shadowing from the vertical support arm for the u_s and v_s corrections (at $\lambda = 30°$ and $60°$ in Fig. 6a,c) and the w_s correction (at $\lambda = 30°$, $60°$ and $\varphi = \pm 60°$ in Fig. 6e); unlike transducer shadowing, the effects of the vertical support arm are slightly visible with the Kaimal corrected anemometer (Fig. 6b,d,f). The relative difference between the posterior corrections without and with the Kaimal shadowing correction (Figs. 5g–i and 7b,d,f) resembles the Kaimal shadowing correction (Fig. 7a,c,e), though the intensities are not the same (Fig. 7a,c,e vs. b,d,f).

Table 1 Relative change in measurements after applying the posterior 3D correction to a vertically mounted anemometer. The u_c, v_c and w_c wind velocity components are in cardinal coordinates (i.e., east, north, up), $\sqrt{u_c^2 + v_c^2}$ is the horizontal speed, T is sonic virtual temperature, σ is the 5-min standard deviation, $\overline{x'T'}$ is the 5-min covariance. Results are summarized as median (95% Bayesian credible interval)

	Standard deviation	Relative change (%)	Covariance	Relative change (%)
ATI 3Vx-probe GLEES experiment without Kaimal shadowing	$\sigma_{\sqrt{u_c^2+v_c^2}}$	9 (5–15)	$\frac{\overline{\left(\sqrt{u_c^2+v_c^2}\right)'T'}}{\overline{w_c'T'}}$	3 (− 3–8)
	σ_{u_c}	1 (− 2–4)	$\frac{\overline{u_c'T'}}{\overline{w_c'T'}}$	0 (− 7–4)
	σ_{v_c}	10 (8–13)	$\frac{\overline{v_c'T'}}{\overline{w_c'T'}}$	12 (8–16)
	σ_{w_c}	$\equiv 0$		
ATI 3Vx-probe GLEES experiment with Kaimal shadowing	$\sigma_{\sqrt{u_c^2+v_c^2}}$	2 (− 1–7)	$\frac{\overline{\left(\sqrt{u_c^2+v_c^2}\right)'T'}}{\overline{w_c'T'}}$	− 2 (− 7–2)
	σ_{u_c}	− 4 (− 6 to − 1)	$\frac{\overline{u_c'T'}}{\overline{w_c'T'}}$	− 5 (− 10 to − 1)
	σ_{v_c}	0 (− 1–1)	$\frac{\overline{v_c'T'}}{\overline{w_c'T'}}$	4 (0–7)
	σ_{w_c}	$\equiv 0$		
Gill R3-50 GLEES experiment	$\sigma_{\sqrt{u_c^2+v_c^2}}$	$\equiv 0$		
	σ_{u_c}	2 (1–3)	$\frac{\overline{u_c'T'}}{\overline{\left(\sqrt{u_c^2+v_c^2}\right)'T'}}$	0 (− 1–0)
	σ_{v_c}	− 3 (− 5 to − 1)	$\frac{\overline{v_c'T'}}{\overline{\left(\sqrt{u_c^2+v_c^2}\right)'T'}}$	− 1 (− 4–1)
	σ_{w_c}	15 (13–18)	$\frac{\overline{w'T'}}{\overline{\left(\sqrt{u_c^2+v_c^2}\right)'T'}}$	8 (6 to 10)
Gill R3-50 Pawnee experiment	$\sigma_{\sqrt{u_c^2+v_c^2}}$	$\equiv 0$		
	σ_{u_c}	− 1 (− 2–1)	$\frac{\overline{u_c'T'}}{\overline{\left(\sqrt{u_c^2+v_c^2}\right)'T'}}$	− 4 (− 7 to − 2)
	σ_{v_c}	− 4 (− 7 to − 1)	$\frac{\overline{v_c'T'}}{\overline{\left(\sqrt{u_c^2+v_c^2}\right)'T'}}$	1 (0–3)
	σ_{w_c}	25 (17–35)	$\frac{\overline{w'T'}}{\overline{\left(\sqrt{u_c^2+v_c^2}\right)'T'}}$	− 6 (− 17–4)

3.2 Non-Orthogonal Anemometer Experiment Over a Subalpine Forest

During the experiment, 710 5-min periods of data were collected with all anemometers vertically mounted (2.5 days), 1174 5-min periods of data were collected during the first manipulation (4.1 days), 1110 were collected during the second manipulation (3.9 days), and 785 were collected during the third manipulation (2.7 days). Each 5-min period contained

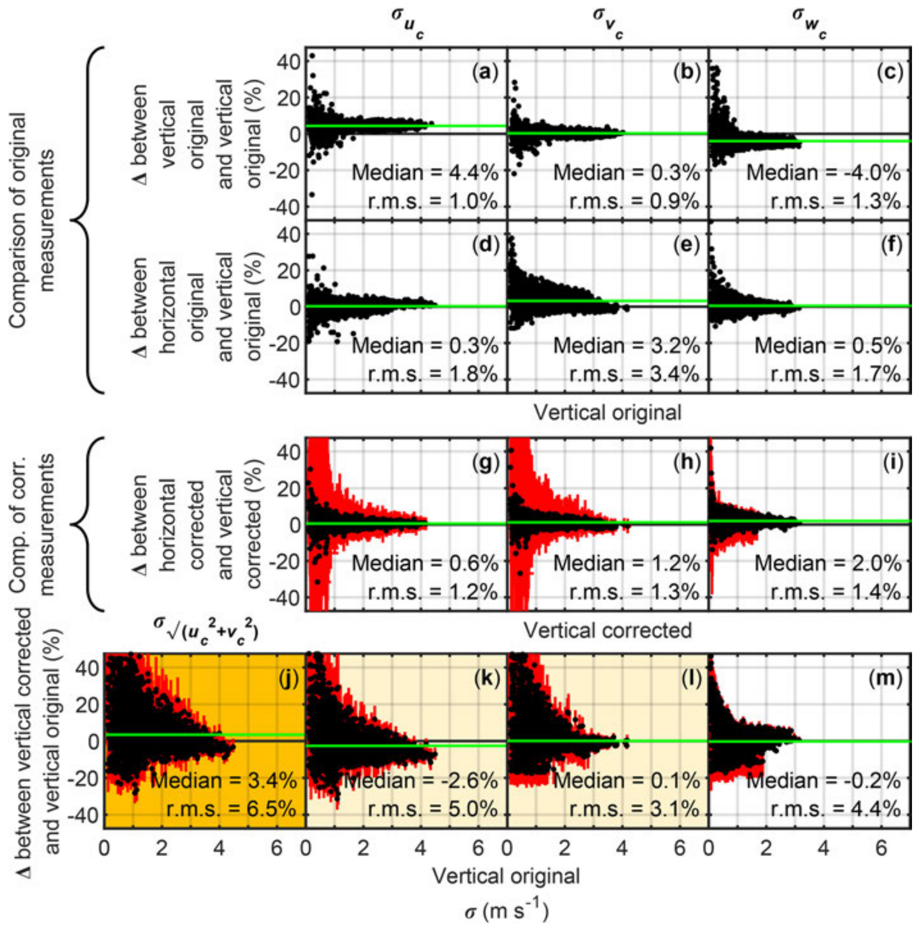

Fig. 4 The same as Fig. 3 but with Kaimal shadowing correction applied before the Bayesian analysis

3000 u_s, v_s, and w_s measurements from three anemometers. In all, the Bayesian analysis evaluated 82,863,000 unique measurements. The number of 10-Hz measurements available for each of the 522 grid points ranged from 17,823 to 1,268,888 (Fig. 3 in the supplementary material). Though no wind directions were excluded from the analysis, airflow was almost exclusively along the axis of the booms and almost never cross-wind between the anemometers (Fig. 3 in the supplementary material). Approximately 12% of the Gill R3-50 temperature data were corrupted for unknown reasons and were omitted from the covariance calculations. The regression slopes of $\overline{u'w'}$ between the three vertically-mounted anemometers were 2% (between positions 1 and 2), 5% (between positions 1 and 3), and 3% (between positions 2 and 3) different from unity while u_* differed by 1% (between positions 1 and 2), 3% (between positions 1 and 3), and 1% (between positions 2 and 3).

For the Gill R3-50 GLEES experiment there were some biases and r.m.s. differences between differently mounted anemometers. The σ_{v_c} measurement was biased − 4.7% with horizontally-mounted anemometers and − 3.2% with tilted anemometers (Fig. 8e, h). The r.m.s. differences for σ_{v_c} and σ_{w_c} between horizontal/tilted versus vertical anemometers

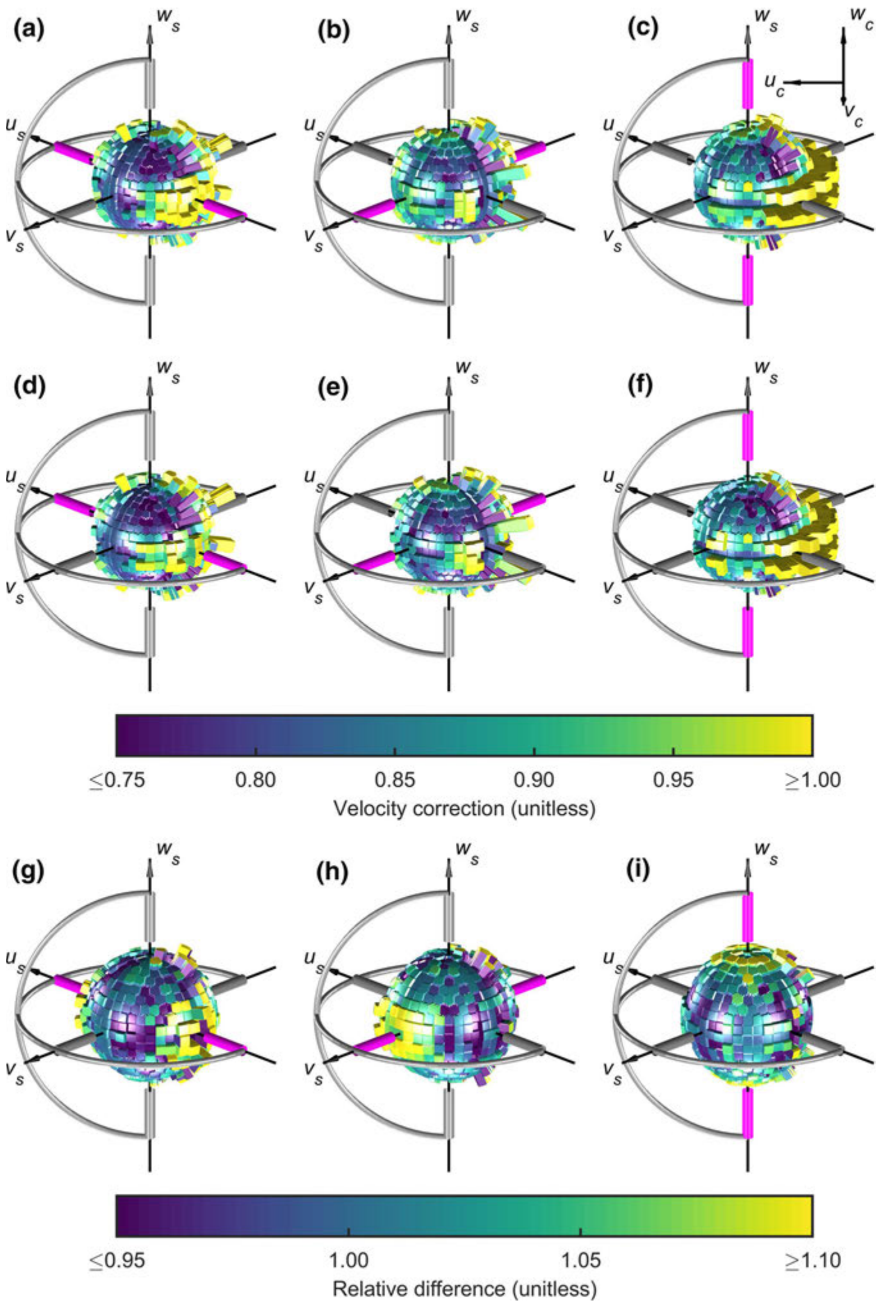

Fig. 5 Bayesian posterior 3D corrections from the ATI 3Vx-probe GLEES experiment. **a**–**c** Without shadowing correction, **d**–**f** with Kaimal shadowing correction applied before the Bayesian analysis, and **g**–**i** the relative difference between without/with Kaimal shadowing correction. In each panel, the correction corresponds to flow originating from various locations and is applied to the velocity component measured with the transducer pair highlighted in magenta. u_s, v_s and w_s are axes in sonic anemometer coordinates with the corresponding u_c, v_c and w_c axes in cardinal coordinates shown in the upper right

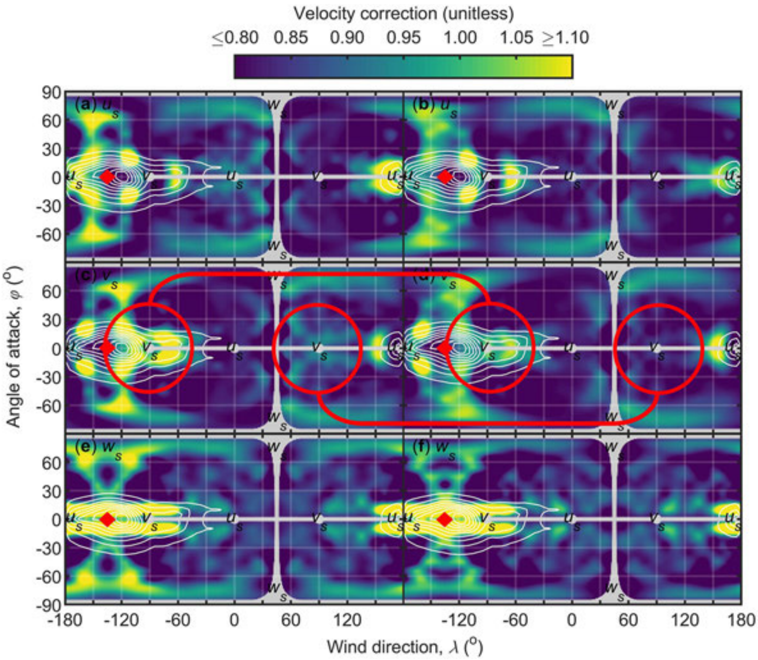

Fig. 6 The Bayesian posterior 3D correction from the ATI 3Vx-probe GLEES experiment. **a**, **c**, **e** Without shadowing correction and **b**, **d**, **f** with Kaimal shadowing correction applied before the Bayesian analysis; the anemometers without Kaimal shadowing correction require additional correction along the u_s and v_s axes (red circles). The correction corresponds to flow originating from various locations and is applied to the u_s, v_s and w_s wind velocity components in orthogonal sonic anemometer coordinates. Wind direction and angle of attack are referenced to the positive u_s axis. The locations of the support structure and transducers are denoted in grey. Contour lines correspond to a histogram of wind directions and angles of attack observed on the vertically-mounted anemometers during the experiment. Wind direction is referenced along the sonic anemometer + u_s axis; in this coordinate system the instrument booms were pointed at − 135° (red diamonds) and potential cross-wind flow obstructions were greatest at − 45° and + 135°. The posterior correction is the same as Fig. 5, though it has been smoothed with a spherical spline

ranged from 2.5 to 3.4% (Fig. 8e,f,h,i), which was greater than similar r.m.s. differences between side-by-side vertical anemometers (1.5–1.8%, Fig. 8b,c). After the Bayesian posterior 3D correction was applied to the 10-Hz time series data, the biases in σ_{v_c} (medians in Fig. 8e,h vs. k,n) and the r.m.s. differences in σ_{v_c} and σ_{w_c} (Fig. 8e,f,h,i vs. k,l,n,o) were effectively removed. When the posterior correction was applied to vertically-mounted anemometers, there was a significant increase in σ_{w_c} (14.5% median difference in Fig. 8s, or alternatively a 15% increase in the regression slope with 13–18% credible interval in Table 1) that was linked to a significant increase in the covariance $\overline{w_c'T'}$ (8% increase in the regression slope with 6–10% credible interval in Table 1); the increase in σ_{w_c} was significantly greater than the increase in $\overline{w_c'T'}$. While the increase in σ_{w_c} did not manifest into a change in the median differences from Fig. 8f,i to l,o, it is apparent in the increase in the range of data on the x-axis where the original σ_{w_c} ranged up to 3.5 m s^{-1} in Fig. 8f,i and the corrected σ_{w_c} ranged up to 4.0 m s^{-1} in Fig. 8l,o (i.e., in order to reduce, in part, the r.m.s. values from 2.5 to 3.4% in Fig. 8f,i to 1.2–1.7% in Fig. 8l,o, the Bayesian analysis had to expand the range of σ_{w_c}). This is in contrast to σ_{v_c}, where the Bayesian analysis was able to reduce both the median and r.m.s. differences (Fig. 8e,h vs. k,n) without increasing the scale of σ_{v_c}, which

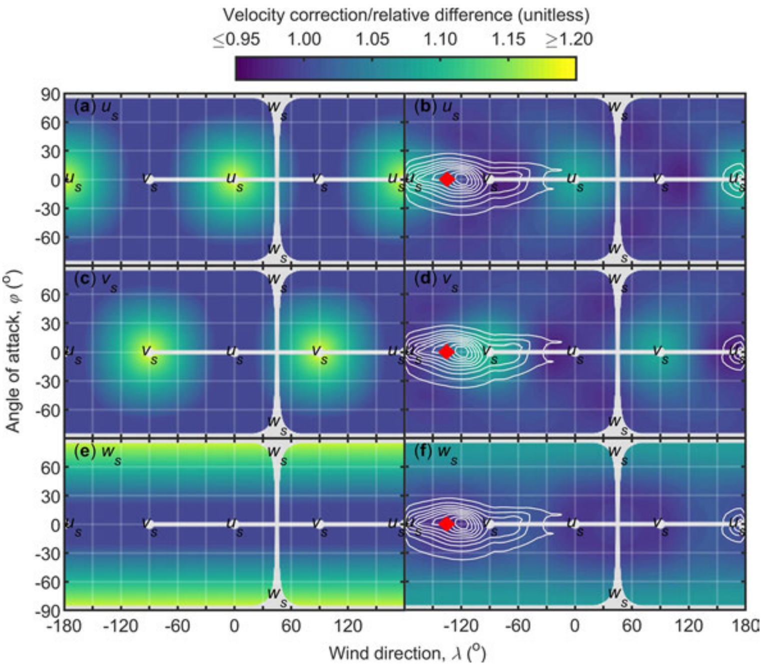

Fig. 7 The ATI 3Vx-probe **a**, **c**, **e** theoretical Kaimal shadowing correction and **b**, **d**, **f** the Bayesian posterior relative difference between without/with Kaimal shadowing correction from the GLEES experiment

is apparent in the x-axis of Fig. 8e,h vs. k,n where it ranged up to 5.5 m s^{-1} before and after the correction. While changes in σ_{u_c} (2.1% median difference in Fig. 8q, or alternatively 2% change in the regression slope with 1–3% credible interval in Table 1) and σ_{v_c} (− 4.2% median difference in Fig. 8r, or alternatively − 3% change in the regression slope with − 5 to − 1% credible interval in Table 1) were statistically significant, they did not correspond to significant changes in the covariances $\overline{u_c' T'}$ or $\overline{v_c' T'}$ (Table 1). Though the posterior correction scaling forces the average horizontal speeds of an upright Gill R3-50 to not change, this does not preclude the possibility that σ_{u_c} and σ_{v_c} can change, but rather, if one increases then the other must decrease to balance out. Had the posterior correction been scaled assuming that the vertical velocity was considered more accurate, then there would have been significant decreases in all of the standard deviations of horizontal velocity components as well as all of the horizontal temperature covariances.

The posterior correction for the Gill R3-50 transducer has regions of intensity generally corresponding to the open areas between the supporting spars and the transducers (Figs. 9, 10a,c,e). Most of this intensity coincides with wind directions and angles of attack experienced by the anemometers during the experiment and the amount of data pooled for each grid location (Fig. 3 in the supplementary material). The posterior correction is not easy to generalize after it is transformed into orthogonal sonic coordinates (Fig. 10b,d,f) and it does not resemble the theoretical Kaimal shadowing correction for an anemometer with the geometry of the Gill R3-50 (Fig. 11).

The analysis of the Gill R3-50 experiment was repeated with validation subsets of the different mountings (e.g., omitting the tilted anemometers and analyzing vertical and horizontal mounted instruments, etc.). For each combination, the Bayesian posterior 3D correction was

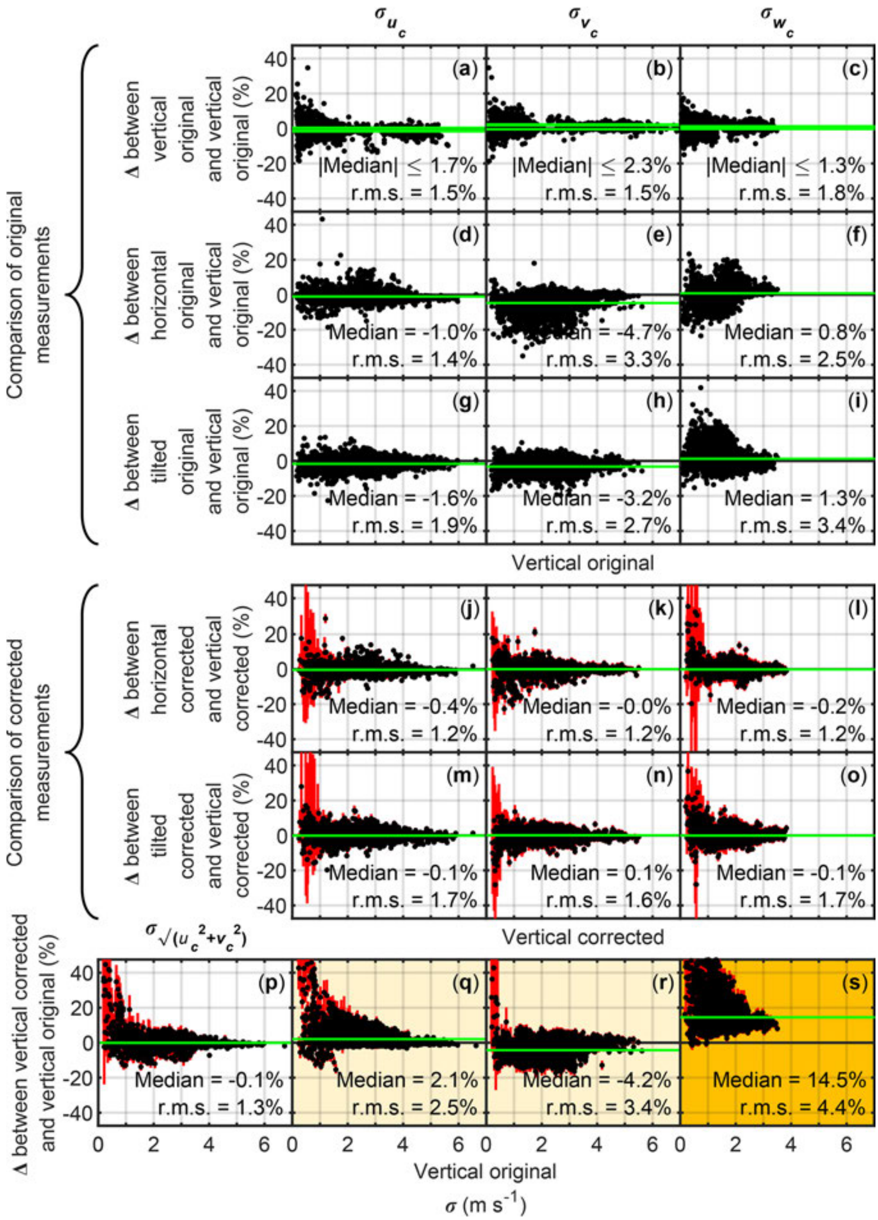

Fig. 8 Results from the Gill R3-50 GLEES experiment comparing σ, the 5-min standard deviation of wind velocity, for vertical, horizontal, and tilted anemometers. u_C, v_C and w_C are velocity components in cardinal coordinates (i.e., east, north, up) and $\sqrt{(u_C^2 + v_C^2)}$ is the horizontal speed. **a–i** Comparison of original u_C, v_C, and w_C measurements between **a–c** vertical anemometers, **d–f** horizontal and vertical anemometers, and **g–i** tilted and vertical anemometers. **j–o** Comparison of u_C, v_C, and w_C measurements after applying the Bayesian posterior 3D correction between **j–l** horizontal and vertical anemometers and **m–o** tilted and vertical anemometers. **p–s** Comparison of original and corrected $\sqrt{(u_C^2 + v_C^2)}$, u_C, v_C, and w_C measurements for vertical anemometers. Results are presented as Δ, the percent relative difference between measurements. The median difference is listed and plotted in green. The root-median-square (r.m.s.) of the residual difference is listed. The 95% Bayesian credible intervals are presented in red

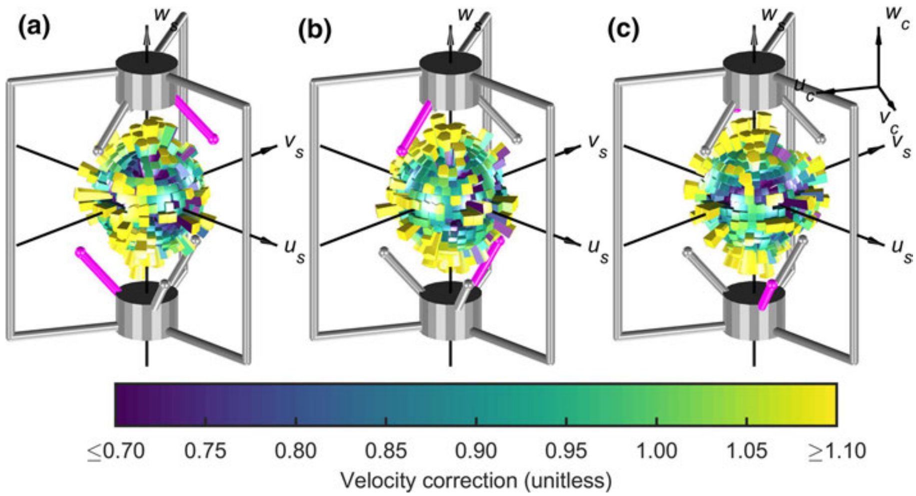

Fig. 9 The Bayesian posterior 3D correction from the Gill R3-50 GLEES experiment. In each panel, the correction corresponds to flow originating from various locations and is applied to the wind velocity component measured with the transducer pair highlighted in magenta. u_S, v_S and w_S are axes in sonic anemometer coordinates with the corresponding u_C, v_C and w_C axes in cardinal coordinates shown in the upper right

then applied to all 10-Hz time series data, including the omitted data. The ability of the posterior correction to predict the anemometers not included in the analyses was quantified similar to Fig. 8j–o (e.g., the r.m.s. difference between tilted-corrected anemometers and vertical-corrected anemometers, though the tilted anemometers were omitted from the analysis that generated the posterior correction). This resulted in 18 comparisons with r.m.s. differences that ranged between 2.0 and 9.7%. For the subset analysis which omitted the vertical anemometers, the largest change when posterior correction was eventually applied to the vertical anemometers was with σ_{w_c} (4% increase in the regression slope with 1–8% credible interval) though the corresponding covariance $\overline{w_c'T'}$ did not change significantly.

3.3 Non-orthogonal Anemometer Experiment Over a Grassland

During the Gill R3-50 Pawnee experiment, 357 5-min periods of data were collected with all anemometers vertically mounted (1.2 days), 116 5-min periods of data were collected during the first manipulation (0.4 days), 282 were collected during the second manipulation (1.0 days), and 113 were collected during the third manipulation (0.4 days). The number of 10-Hz measurements available for each of the 522 grid points ranged from 1018 to 561,415 (Fig. 4 in the supplementary material). Wind directions were bimodal, with a majority of airflow from behind the structure along the axis of the booms (i.e., − 120° in Fig S4) and with some from the left of the booms, though almost never cross-wind between the anemometers (Fig. 4 in the supplementary material). The regression slopes of $\overline{u'w'}$ between the three vertically-mounted anemometers were 19% (between positions 1 and 2), 16% (between positions 1 and 3), and 1% (between positions 2 and 3) different from the 1:1 line while u_* differed by 10% (between positions 1 and 2), 8% (between positions 1 and 3), and 0% (between positions 2 and 3). Results were contradictory. After the Bayesian posterior 3D correction was applied to the 10-Hz time series data, vertically-mounted anemometers experienced an increase in σ_{w_c} (25.4% median difference in Fig. 5s in the supplementary material, or

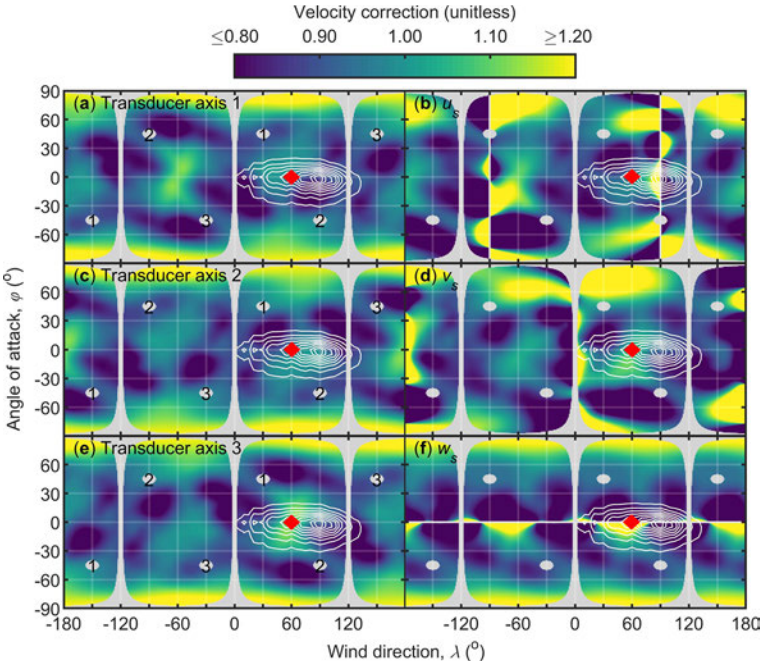

Fig. 10 The Bayesian posterior 3D correction from the Gill R3-50 GLEES experiment. The correction corresponds to flow originating from various locations and is applied to **a**, **c**, **e** the wind velocity component measured with each transducer pair in non-orthogonal transducer coordinates or **b**, **d**, **f** the u_s, v_s and w_s velocity components in orthogonal sonic anemometer coordinates. Wind direction and angle of attack are referenced to the positive u_s axis. The locations of the support structure and transducers are denoted in grey. Contour lines correspond to a histogram of wind directions and angles of attack observed on the vertically-mounted anemometers during the experiment. Wind direction is referenced along the sonic anemometer + u_s axis; in this coordinate system the instrument booms were pointed at 60° (red diamonds) and potential cross-wind flow obstructions were greatest at − 30° and + 150°. The posterior correction in **a**, **c**, **e** is the same as Fig. 9, though it has been was smoothed with a spherical spline

alternatively a 25% increase in the regression slope with 17–35% credible interval in Table 1) while $\overline{w_c'T'}$ did not change significantly (Table 1). The changes in σ_{u_c}, $\overline{u_c'T'}$, σ_{v_c}, and $\overline{v_c'T'}$ were much smaller but similarly contradictory (Table 1). In this experiment the posterior correction had very few regions of intensity (Figs. 6 and 7a,c,e in the supplementary material), though these generally coincided with wind directions and angles of attack experienced by the anemometers during the experiment and the amount of data pooled for each grid location (Fig. 4 in the supplementary material). Had the posterior correction been scaled assuming that the vertical velocity was considered more accurate, then there would have been significant decreases in all of the standard deviations of horizontal velocity components, but no significant changes in any of the horizontal temperature covariances.

4 Discussion

4.1 Interpreting Posterior Three-Dimensional Corrections

Regions of intense correction in the Bayesian posteriors for both the ATI 3Vx-probe and the Gill R3-50 are generally in locations corresponding to the amount of data collected by

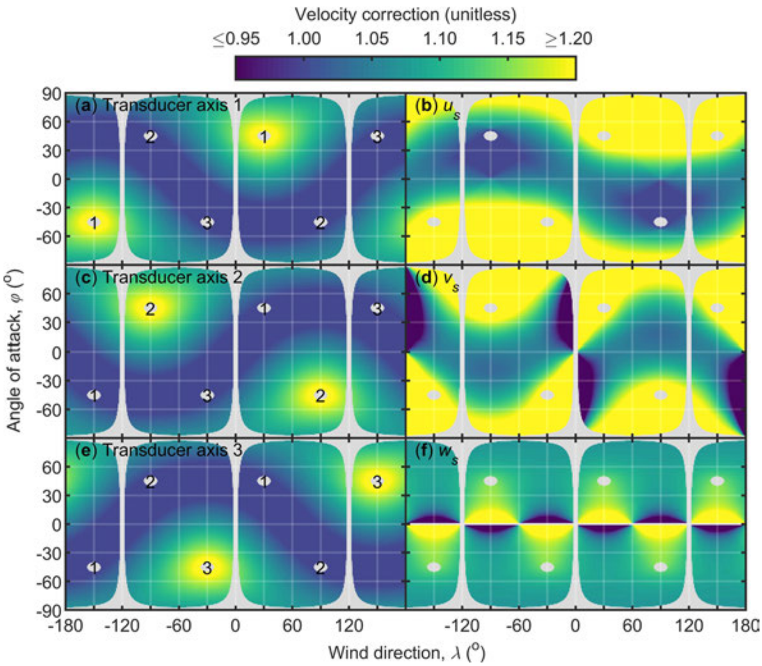

Fig. 11 The theoretical Kaimal shadowing correction for the Gill R3-50 geometry. The correction corresponds to flow originating from various locations and is applied to **a**, **c**, **e** the wind velocity component measured with each transducer pair in non-orthogonal transducer coordinates or **b**, **d**, **f** the u_s, v_s and w_s velocity components in orthogonal sonic anemometer coordinates. Wind direction and angle of attack are referenced to the positive u_s axis. The locations of the support structure and transducers are denoted in grey

the anemometers at the field sites during the experiments (Figs. 6, 10a,c,e and 7a,c,e in the supplementary material vs. Figs. 2–4 in the supplementary material). This is counter to our hypothesis (1) that the posterior correction for the ATI 3Vx-probe without the Kaimal shadowing correction should coincide with flow across the transducers or structures, which was the case for the CSAT3 in Frank et al. (2016a). While this is discouraging, we believe there are several distinctions between our study and Frank et al. (2016a) that could explain why the posterior corrections appear differently.

First, we use less assumptions of symmetry and conversely more process parameters to characterize the 3D space around the anemometers. For the CSAT3, Frank et al. (2016a) assumed that the effect of the upper and lower mounting arms that extend back into the support block is negligible, which, through symmetry, permitted a solution using 138 parameters that uniquely characterized only a quarter of the sphere around one transducer pair. The ATI 3Vx-probe and the Gill R3-50 both have supporting structures that are likely to affect the measurements but are not symmetrical with respect to the transducer axes. Thus, the solution for the Gill R3-50 required 256 parameters to uniquely characterize a hemisphere around the transducers (i.e., the top half of Fig. 10a which is repeated throughout Fig. 10a,c,e) while the ATI 3Vx-probe required 428 parameters and a separate solution for the hemisphere around the w_s axis (i.e., the top half of Fig. 6e is different than the top half of Fig. 6a, c). With fewer instances of symmetry there is less pooling of data from which the Bayesian analysis can estimate a correction. The ATI 3Vx-probe, which assumed the least symmetry, required the most parameters, and experienced the fewest manipulations (vertical and horizontal anemometers only), had the most irregular posterior correction. If the supporting structures of both anemometers are neglected, then the flow distortions around the transducers are symmetrical and more grid points can be pooled (i.e., the correction for the ATI 3Vx-probe u_s and v_s transducers can be combined with w_s in Fig. 6., resulting in left–right symmetry around each transducer in Figs. 6 and 10 and 7 in the supplementary material). This would better distribute the available data (i.e., the "+" in Fig. 2 in the supplementary material would appear in the gaps between each u_s/v_s, u_s/w_s, and v_s/w_s transducer pair and the "*" that appears in Fig. 3 in the supplementary material would be top–bottom and left–right symmetrical as well as duplicated within the gaps that are located under the vertical supporting arms) and could possibly result in more interpretable posterior 3D corrections, as in Frank et al. (2016a). We specifically chose not to do this, because to do so would be to eliminate the possibility of quantifying shadowing from the support structures. We acknowledge this is a trade-off, and regard the ability to account for structural shadowing as more important than producing a more robust, omnidirectional, and universally applicable correction.

Second, it is possible that the pattern of intense correction corresponding to the histogram of wind directions and angles of attack reflects a type of "overfitting" of the statistical model (Hawkins 2004). Overfitting occurs when an analysis is fit too closely to a dataset, resulting in a statistical model that is remarkably poor at predicting similar but different data. Often this is associated with analyses that have too many statistical parameters. For the ATI 3Vx-probe and Gill R3-50, there are a small number of statistical parameters defining the 3D corrections, 428 and 256, compared to a large amount of high frequency measurements, 106,704,000 and 82,863,000. Yet, the Bayesian likelihood is based on predicting the 17,778 and 27,621 5-min standard deviations with 8889 and 9207 process parameters representing the "true" standard deviations of velocity components for the ATI 3Vx-probe and Gill R3-50 respectively. In these experiments there were about 10,000 times more data than process parameters. Due to the complexity of these Bayesian analyses it is difficult to assess whether this could lead to overfitting. The r.m.s. differences between anemometers provide evidence that the data are too closely predicted by the statistical model: the posterior corrected vertical, horizontal, and titled anemometers appear more similar to each other (0.8–1.4% for the ATI 3Vx-probe in Figs. 3g–i and 4g–i, 1.2–1.7% for the Gill R3-50 GLEES experiment in Fig. 8j–o, 1.7–2.2% for the Gill R3-50 Pawnee experiment in Fig. 5j–o in the supplementary material) than side-by-side vertically-mounted anemometers deployed as they were designed (0.9–1.3% for the ATI 3Vx-probe in Fig. 4a–c, 1.5–1.8% for the Gill R3-50 GLEES experiment in Fig. 8a–c, 2.3% for the Gill R3-50 Pawnee experiment in Fig. 5a–c in the supplementary material). Also, the Bayesian analyses are remarkably poor at predicting different data, as illustrated by the validation subset analyses of different Gill R3-50 mountings. Applying the posterior corrections to data omitted from these analyses increased the r.m.s. differences between anemometers to 2–10%. In the case where the vertical anemometer is omitted from the analysis, when the resulting posterior correction is applied to the vertical data it resulted in a small change in σ_{w_c} (1–8% credible interval) but not a statistically significant change in $\overline{w_c'T'}$. When the posterior correction is applied from the GLEES results to the Pawnee data, and vice versa, the differences between the anemometers are exacerbated (results not shown). This is not the case with the CSAT3 in Frank et al. (2016a), where the posterior correction from the GLEES experiment was applied to data collected above a short grass pasture in Colorado, which significantly reduced the bias in σ_{v_c} measurements between vertically and horizontally-mounted anemometers (there was no significant change with σ_{v_c} or σ_{w_c}). That study also included an "askew" mounting in the pasture dataset that was not improved with the posterior correction; unlike our results, their application to a "new" mounting did not make the discrepancies worse.

Overfitting could also explain why changes in the standard deviations are not always linked to changes in the corresponding covariances. The random error of a covariance is proportional to the product of the random errors of its two constituents (Geissbühler et al. 2000). If the increased variability in wind velocity due to overfitting is random, then the covariance with temperature, which is not affected by the posterior correction, will have a much smaller random error. While it is unclear what proportion of the 15% increase in σ_{w_c} from the Gill R3-50 GLEES experiment could be associated with statistical overfitting, the corresponding 8% increase in $\overline{w_c' T'}$ indicates that the posterior correction (Fig. 10f) has some systematic structure relative to turbulent transport. We suspect that each of the posterior corrections exhibit some amount of overfitting because the changes in the covariances were smaller than the corresponding changes in standard deviations (the only exception was $\overline{v_c' T'}$ which increased more than σ_{v_c} in the Gill R3-50 Pawnee experiment). By definition the posterior correction was normalized to force zero change in σ_{w_c} (for the ATI 3Vx-probe) or $\sigma_{\sqrt{u_c^2+v_c^2}}$ (for the Gill R3-50), yet the corresponding covariances $\overline{w_c' T'}$ and $\left(\sqrt{u_c^2 + v_c^2}\right)' T'$ decreased by − 4 and − 3% (note, these are essentially the scaling factors used in the covariance column in Table 1).

We do not believe that cross-wind flow distortion between the sonic anemometers or from the tower significantly influenced these results, especially for the GLEES experiments. First, for the ATI 3Vx-probe and Gill R3-50 GLEES experiments airflow was almost exclusively into the booms with the tower behind and almost never cross-wind from one anemometer into another (Figs. 2, 3 in the supplementary material). At the Pawnee site, airflow was mostly from behind the structure and almost never cross-wind through the anemometers (Fig. 4 in the supplementary material). While the easterly wind directions were unexpected, the anemometers were mounted well above a relatively uncluttered structure (Fig. 1 in the supplementary material). Second, the differences in friction velocity between side-by-side vertically-mounted anemometers was small, with the regression slopes between ATI anemometers being only 1.02 (i.e. 2% different from unity) while the differences in slopes among the three Gill R3-50 s was 1%, 3%, and 1%. By comparison, these differences are similar if not smaller than found in other field intercomparisons where replicate anemometers were mounted over relatively flat terrain on slimmer towers with much wider lateral spacing (i.e., more ideal for reducing cross-wind and tower related flow distortions). In Mauder et al. (2007), u_* from three CSAT3s were tested, and the regression slopes between the second and third anemometers compared against the first were 1% and 2% different from unity. In Mauder and Zeeman (2018), u_* from two CSAT3s were tested against an intermediary Gill HS anemometer, with the regression slopes of 0.91 and 0.95 indicating the difference between the CSAT3s was on the order of 4%. For the Gill R3-50 GLEES experiment, the measurement path centres of the rotated anemometers could not be manipulated to the exact height. While it is possible that these differences in height could lead to an error in the analysis, considering the canopy averaged 7 m and the relative difference in height above the canopy between locations 1 and 2 was − 0.4% and between locations 1 and 3 was 1.0%, we assume this had a minimal impact on the results.

Nevertheless, the posterior corrections do contain meaningful information. The most powerful example is to consider the different ATI 3Vx-probe results between the dataset that did not receive the Kaimal shadowing correction and the one that did. In both cases the prior probability distributions for the corrections were defined with means equal to 1 (i.e., uniformed priors), resulting in Bayesian analyses that treated these as two arbitrary and unrelated datasets. Yet, the posterior corrections were not arbitrary and unrelated, as there is clearly structure in the relative difference between them (Figs. 5g–i and 7b,d,f), which has a remarkable resemblance to the Kaimal shadowing correction (Fig. 7a,c,e). This is a powerful validation of our methodology and statistical model, because the only result of this study that was known a priori was that these two datasets differ by the absence/presence of the Kaimal shadowing correction; this was subsequently confirmed a posteriori by the Bayesian analysis.

In summary, the 3D corrections in this study must be interpreted with caution. As they may be overfitted to our datasets, we do not recommend that they be applied elsewhere. But, we do believe they are applicable to and help explain our experiments. With careful consideration of the relative changes in standard deviations and corresponding covariances, they can give meaningful insights into the accuracy of orthogonal and non-orthogonal sonic anemometers.

4.2 Orthogonal Anemometer

The performance of the ATI 3Vx-probe orthogonal anemometer was consistent with expectations based on prior studies. In Kaimal et al. (1990), two uncorrected ATI probes angled 45° apart measured very different horizontal velocity components, a problem that was remedied by applying a transducer-shadowing correction based on Kaimal (1979). Our experiment was similar, where the u_s and v_s transducers of the vertically/horizontally mounted anemometer were 45° from the w_s transducers of the horizontally/vertically mounted instrument; i.e., differences between vertically and horizontally-mounted anemometers along the cardinal v_c and w_c axes are directly comparable to Kaimal et al. (1990). As expected, we observed clear biases in measurements along these axes when these were calculated without the Kaimal shadowing correction (Fig. 3e,f) that were mitigated when we applied this manufacturer recommended correction (Fig. 4e,f). When the posterior 3D correction was applied to a vertically mounted ATI 3Vx-probe without the Kaimal shadowing correction, the σ_{v_c} deviation and $\overline{v_c'T'}$ covariance increased about 10% relative to σ_{w_c} and $\overline{w_c'T'}$(Fig. 3l vs. m, Table 1) which led to roughly a 10% increase in $\sigma_{\sqrt{u_c^2+v_c^2}}$ relative to σ_{w_c} (Fig. 3j vs. m, Table 1). This is consistent with the interpretation of Kaimal et al. (1990) and Frank et al. (2016b) that ATI anemometers without shadowing correction substantially underestimate horizontal speed. A possible reason for the lack of increase in $\overline{\left(\sqrt{u_c^2+v_c^2}\right)'T'}$ (non-significant credible interval, Table 1) could be that by orienting the anemometers into the approximate mean wind direction the $\overline{u_c'T'}$ covariance was much stronger than $\overline{v_c'T'}$ and the former was minimally affected by the posterior correction. In the case of the ATI 3Vx-probe with Kaimal shadowing correction applied before the Bayesian analysis, the resulting posterior 3D correction did not change $\sigma_{\sqrt{u_c^2+v_c^2}}$, σ_{v_c}, $\overline{\left(\sqrt{u_c^2+v_c^2}\right)'T'}$, and $\overline{v_c'T'}$ (non-significant credible interval, Table 1), though σ_{u_c} and $\overline{u_c'T'}$ are slightly biased (− 6 to − 1% and − 10 to − 1% credible intervals, Table 1). Overall, these results indicate that an ATI orthogonal anemometer with Kaimal shadowing correction has little relative bias between the horizontal and vertical dimensions, which is a similar finding to Frank et al. (2016b). Had we not assumed that the most accurate measurement on the ATI 3Vx-probe was the vertical speed, and instead scaled the 3D posterior correction to not change the horizontal velocity, our interpretation of the Kaimal corrected anemometer would be unchanged. Therefore, we retain our hypothesis (1).

Historically, orthogonal transducer shadowing has been corrected with simple functions (Kaimal 1979; Wyngaard and Zhang 1985) that have been corroborated by modern experiments (Ghaemi-Nasab et al. 2018). While the posterior corrections from our analyses are difficult to interpret, transducer shadowing is most apparent in Fig. 6 (i.e., comparing within the red circles in panel c which has more correction versus d which has less correction, especially along the v_s axis). It is possible that the regions of intensity that appear to coincide with the support structure (at $\lambda = 30°$ and $60°$ in Fig. 6a, c and at $\lambda = 30°$, $60°$ and $\varphi = \pm 60°$ in Fig. 6e) are related to shadowing from support structure. To our knowledge, this phenomena has not been quantified in other studies.

It is difficult to directly assess the accuracy of the ATI 3Vx-probe, though it is clear that the original horizontal speed requires roughly a 10% correction. For our data, the simple application of the Kaimal shadowing correction caused average increases in σ_{u_s} and σ_{v_s} of 8 and 10%. Yet, Kaimal-corrected horizontal velocity measurements can be compared to objective standards, such as comparing mean velocities to those from propeller anemometers (Kaimal et al. 1990), and with which orthogonal ATI anemometers have compared favorably against other anemometers (Loescher et al. 2005; Mauder et al. 2007, Frank et al. 2016b). Meanwhile, the Kaimal shadowing correction caused w_s to increase only an average of 2% due to the limited range of angles of attack at the GLEES field site (Fig. 6); had the ATI 3Vx-probe been deployed at the Pawnee site the average vertical correction would have been even smaller due to the extremely small angle of attack range (Fig. 7 in the supplementary material). Considering the Kaimal shadowing correction is small for w_s and there is little bias between the horizontal and vertical dimensions of a manufacturer corrected anemometer, we deduce that the vertical velocity from the orthogonal anemometer is reasonably accurate.

4.3 Non-orthogonal Anemometer

Though the Gill R3-50 non-orthogonal anemometer is manufacturer calibrated, our results bring into question the accuracy of its vertical velocity measurement and raise the possibility that its vertical fluxes are underestimated. In the analysis of our GLEES experiment, the posterior correction changed the vertical velocity such that σ_{w_c} significantly increased by 13–18% which corresponded to a 6–10% increase in $\overline{w_c'T'}$ (Table 1). We must consider that had we not assumed that the most accurate measurement of the Gill R3-50 is the horizontal speed, and instead scaled the 3D posterior correction to not change the vertical velocity, our interpretation would be the opposite. Thus, taken independently, our results indicate that either the horizontal velocity is overestimated or the vertical velocity is underestimated. Since the horizontal speed of the Gill R3-50 are specifically calibrated in an ISO 16622 traceable wind tunnel (Gill Instruments Limited 2017), we consider it unlikely that the horizontal velocity components are significantly underestimated. Therefore, we retain our hypothesis (2).

Unfortunately, the exact cause for this is difficult to ascertain. The details of the angle of attack based look-up table correction for the Gill R3-50 are proprietary, though an earlier manual states: “If operating in a calibrated mode a correction operation is then applied to calibrate out the affects of the transducers and head framework” (Gill Instruments Limited 2005). Based on confirmation with the manufacturer that, to a degree, this correction addresses transducer shadowing, it is not unreasonable to suspect that it has a vague resemblance to the theoretical Kaimal shadowing correction for a non-orthogonal anemometer with 45° titled transducers (Fig. 11). Yet, it is obvious that our results (Figs. 9 and 10) are dissimilar to this theoretical Kaimal shadowing correction (Fig. 11). This is because the Bayesian analysis corrects an already corrected anemometer, such that there is no a priori knowledge of what our posterior corrections should look like (Figs. 9 and 10). The intense shadowing at the top and bottom of the structure (i.e., $|\varphi| > 60°$ in Fig. 10) is consistent with large angle of attack errors found in other Gill anemometers (Nakai and Shimoyama 2012). Yet, these errors cannot explain the increases in σ_{w_c} and $\overline{w_c' T'}$ that occurred at much narrower angles of attack (i.e., angle of attack histogram between $|\varphi| < 32°$ in Fig. 10).

4.4 Coordinate Rotation Amplifies Uncertainty and Bias in Non-orthogonal Sonic Anemometer Vertical Wind Speeds

A recent sonic anemometer intercomparison demonstrated that several commonly used non-orthogonal instruments produced similar wind measurements, including the standard deviation of vertical velocity and buoyancy flux (i.e., proportional to $\overline{w' T'}$) (Mauder and Zeeman 2018). Is it plausible, if not probable, that these anemometers are all "afflicted with an error of almost the exact same magnitude"? A considerable amount of literature has been devoted to investigating errors in the non-orthogonal CSAT3, an anemometer that the manufacturer forthrightly discloses has no shadowing correction applied to its default measurements. This simplifies our understanding of its measurements and has led to different approaches used to detect underestimates in vertical velocities (Horst et al. 2015; Frank et al. 2016a; Huq et al. 2017; Peña et al. 2019). Yet our ability to understand and test non-orthogonal anemometers that are manufacturer calibrated is more complicated. Grare et al. (2016) used, in part, an intercomparison with a CSAT3 to demonstrate that the Gill R3-50 horizontal speed is accurate; they also confirmed this with an independent wind tunnel test similar to what Friebel et al. (2009) had done to demonstrate the accuracy of the CSAT3 horizontal measurement. Yet, with no clear objective standard with which to test the vertical velocity against, potential errors are difficult to detect. One approach is through manipulation experiments using replicate anemometers. Kochendorfer et al. (2012) tested the R.M. Young 81,000 (a non-orthogonal anemometer with transducers tilted $\pm 45°$ and manufacturer corrected) and evaluated vertical velocity errors associated with various small angles of attack (i.e., $|\varphi| \leq 15°$) and found mean corrections ranged between 0 and 16%. Nakai and Shimoyama (2012) tested the Gill WindMaster (another non-orthogonal anemometer with transducers tilted $\pm 45°$ and manufacturer corrected), and though their results are focused on large angles of attack, their data from $\varphi = \pm 10°$ suggests that vertical velocity might be underestimated; note, this anemometer has since been the subject of a "*w*-boost" firmware bug (Billesbach et al. 2019). A new approach is to investigate the power spectra of vertical and horizontal velocity components within the inertial subrange, which Peña et al. (2019) did to show the Metek USA-1 (a non-orthogonal anemometer with transducers tilted $\pm 45°$) achieves a theoretical ratio once the manufacturer recommended correction is applied.

One commonality of all non-orthogonal anemometers is that if any systematic errors occur in the transducer measurements then the error in the vertical velocity measurement is uncertain and unpredictable for small angles of attack. This was proposed by Frank et al. (2016a) for the CSAT3 and is similarly derived for non-orthogonal anemoemters with transducers tilted $\pm 45°$ in the "Appendix". For anemometers including the Gill R3-50, the limit of the vertical velocity correction as the angle of attack becomes near-horizontal is

$$\lim_{\varphi \to 0} \frac{\hat{w}_s}{w_s} = \frac{\alpha_1(\lambda, \varphi) + \alpha_2(\lambda, \varphi) + \alpha_3(\lambda, \varphi)}{3} + \left(\frac{\sqrt{3}\cos\lambda + \sin\lambda}{6}\alpha_1(\lambda, \varphi) - \frac{\sin\lambda}{3}\alpha_2(\lambda, \varphi) + \frac{-\sqrt{3}\cos\lambda + \sin\lambda}{6}\alpha_3(\lambda, \varphi) \right) \lim_{\varphi \to 0} \frac{1}{\tan\varphi}, \quad (5)$$

where the transducer corrections (α_1, α_2, and α_3) are functions of wind direction and angle of attack (i.e., Figs 10a,c,e and 7a,c,e in the supplementary material). This limit will approach $\pm\infty$ for most functions of α, unless $\alpha_1 \equiv \alpha_2 \equiv \alpha_3$ near the horizontal plane (which has a special case where all are constant). A consequence of this is that there will almost assuredly be an angle of attack range over which the accuracy of the vertical velocity measurement is unpredictable; accurately estimating the angle of attack range is extremely difficult as well, as it requires a precise and accurate knowledge of the "true" transducer corrections required for near-horizontal flows. There are two limitations for evaluating this for the Gill R3-50: the "true" correction is unknown and details of the angle of attack look-up table correction applied by the manufacturer are not publically available. The "true" correction might be unknowable to the precision required to adequately reduce the vertical velocity uncertainty of near-horizontal flows. A sufficient correction would require a detailed 3D understanding of shadowing from the transducers and structure. It would also need to consider that shadowing responds to secondary effects such as wind velocity (Horst et al. 2015), which can manifest under high wind speeds and delay the time of flight between the transducers, (Burns et al. 2012) as well as wind rotation (Ghaemi-Nasab et al. 2018), which indicates that the interaction of swirling eddies on the outgoing/incoming time of flight measurements might be important. As described in the previous section, it is not unreasonable to suspect that both the "true" correction and the look-up table have vague resemblances to the theoretical Kaimal shadowing correction for a non-orthogonal anemometer with 45° titled transducers in Fig. 11. Therefore, we make a rudimentary estimation of the uncertainty of the vertical velocity by performing a sensitivity test of the theoretical Kaimal shadowing correction for the Gill R3-50 geometry. There are two generally accepted formulations for this correction, a piecewise function proposed by Kaimal (1979) or a sinusoidal function proposed by Wyngaard and Zhang (1985), and both have been applied to the non-orthogonal CSAT3 (Horst et al. 2015; Frank et al. 2016b; Huq et al. 2017). For the Gill R3-50, $L/d = 14$ leads to a maximum correction of 21% (Wyngaard and Zhang 1985) and these functions become $x_s = (0.79 + 0.21\theta/75)\,\hat{x}_s$ for $\theta \leq 75°$, otherwise $x_s = \hat{x}_s$ for $\theta > 75°$ versus $x_s = (0.79 + 0.21\sin(\theta))\,\hat{x}_s$. Figure 11 shows the theoretical correction using the piecewise function while Fig. 12 shows the resulting sensitivity caused by selecting one formulation over another. The differences are minimal in transducer coordinates (maximum difference of 2.8%, Fig. 12a,c,e) and for the u_s and v_s measurements (Fig. 12b,d) but can be $>5\%$ for w_s for angles of attack within $|\varphi| \leq 13.6°$ (Fig. 12f). Even though the posterior corrections for the Gill R3-50 were difficult to interpret, the w_s corrections for the GLEES and Pawnee experiments (Figs. 10f and Fig. 7f in the supplementary material) demonstrate remarkable similarities to Fig. 12f for near-horizontal flows. Ultimately, we suspect that the contradictory results from our Pawnee experiment were due to complications from all angles of attack being between $|\varphi| \leq 11°$ (Fig. 7 in the supplementary material).

If the uncertainty in choosing between a piecewise versus sinusoidal correction represents a plausible uncertainty in the manufacturer's ability to accurately and precisely calibrate/correct the transducer measurements, then all vertical velocity measurements with angles of attack between $\pm 13.6°$ should be treated with suspicion (note, calculations based on the largest diameter of the tapered Gill R3-50 transducer, such that $L/d = 13$, increase this range to $\pm 15.3°$). This is alarming, as the choice of a piecewise versus sinusoidal function is generally uncontroversial and typically has minimal effect on results (Frank et al. 2016a; Huq et al. 2017). The total uncertainty in this region can be biased, as demonstrated in Fig. 12f where the angles of attack with $< -5\%$ difference only occur between $|\varphi| \leq 4.8°$. This can explain how σ_{w_c} and $\overline{w_c' T'}$ could be underestimated: from some wind directions the upwelling eddies could be underestimated more than the downwelling eddies are overestimated leading

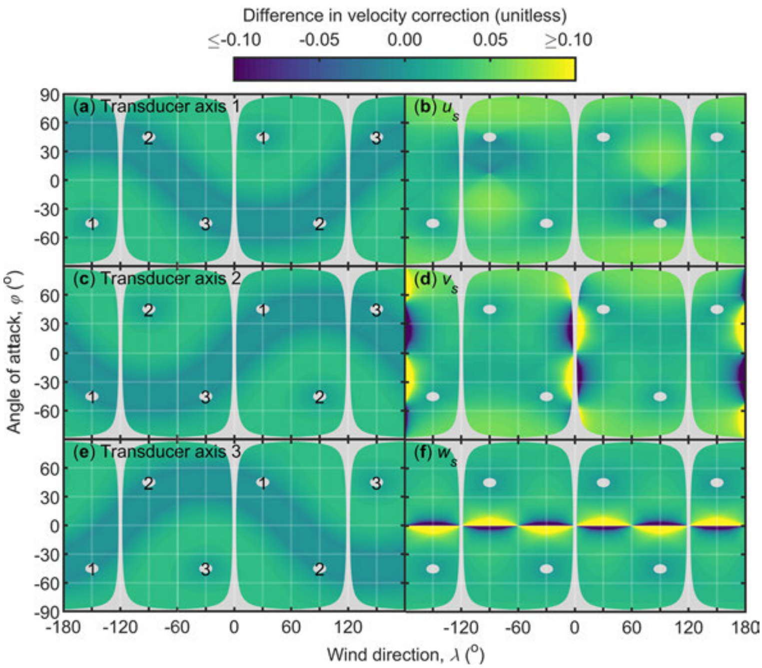

Fig. 12 The difference in the wind velocity correction between two formulations of the theoretical Kaimal shadowing correction for the Gill R3-50 geometry: a piecewise function (Kaimal 1979) versus a sinusoidal function (Wyngaard and Zhang 1985). The correction corresponds to flow originating from various locations and is applied to **a**, **c**, **e** the velocity component measured with each transducer pair in non-orthogonal transducer coordinates or **b**, **d**, **f** the u_s, v_s and w_s velocity components in orthogonal sonic anemometer coordinates. Wind direction and angle of attack are referenced to the positive u_s axis. The locations of the support structure and transducers are denoted in grey

to lower variance and less upwelling warm air, while from other wind directions downwelling eddies could be underestimated more than upwelling eddies are overestimated leading also to lower variance as well as less downwelling cold air. It must be noted, that had we switched the roles of the piecewise versus sinusoidal functions in the sensitivity analysis, the results would still be biased, though towards overestimates. This means that if the non-orthogonal transformation plays a role in the possibility that multiple non-orthogonal sonic anemometers underestimate vertical velocities, then the differences between the "true" corrections and manufacturers' corrections are not random; rather, there is some systematic bias towards characterizing the transducer measurements. While this might seem implausible, as shown by Fig. 12, this can occur with only a 1–2% transducer measurement error; it is conceivable that such a small bias might occur among all manufacturers if there were a general trend to under-correcting a source of shadowing (i.e., from the structure or the other transducers) or from a secondary source of error that is generally neglected.

Based on this sensitivity test, we make the following conclusions: (1) Unless a manufacturer correction to characterize the "true" shadowing and flow distortion around the transducer for near-horizontal flows is significantly better than the uncertainty in this sensitivity test, it is plausible, if not probable, that anemometers with the geometry of the Gill R3-50 will have vertical velocity errors with magnitudes > 5% for angles of attack between at least ± 14°. (2) These errors can be biased either positive or negative such that when applied to an actual dataset these errors will not necessarily average out. (3) These consequences are deduced from a geometry with transducers tilted ± 45° from horizontal and should apply to all anemometers tested in Mauder and Zeeman (2018) except the CSAT3, which is titled ± 60°; while different anemometers will have different *L*/*d* ratios which would result in different uncertainties, the general principle would be the same. Therefore, we retain our hypothesis (3) that the mathematics of the non-orthogonal geometry can plausibly cause innocuous errors in transducer measurements to be transformed into significant systematic errors in vertical velocities. Finally, because these uncertainties fundamentally approach $\pm\infty$ (Eq. 5), they may be extremely difficult to adequately correct.

4.5 Future Research

Regardless of the interpretation of our field experiments, the ramifications of our finding of the non-orthogonal transformation as a source uncertainty and enhancement of error in the vertical wind velocity merits further investigation. With technological advancements, it might be possible to test for these errors when previously no measurement standard had existed. An emerging technology is Doppler lidar, which can provide an independent velocity measurement without causing flow distortions (Mauder et al. 2019). Considering that potential uncertainties and underestimates in vertical velocity due to the non-orthogonal transformation involve small transducer errors and small angles of attack, future testing might be best conducted in a large wind tunnel. In such a test, a series of optical paths using Doppler lidar could be oriented to exactly replicate the transducer geometry of the Gill R3-50, ATI Vx-probe, CSAT3, etc., and a series of optical paths could be aligned with the sonic u_s, v_s, and w_s axes to confirm the accuracy of the measurements in both transducer and sonic coordinates (a third set of optical paths aligned in wind-tunnel coordinates would also be beneficial). A sonic anemometer could be mounted for easy removal and aligned with the Doppler lidar axes, such that under turbulent flow a series of measurements could be made alternatively with the anemometer and then with the Doppler lidar. This could be repeated for various wind directions (i.e. rotating the anemometers and Doppler lidar) and with small increments of angles of attack. Under these conditions, it might be possible to accurately define the region of near-horizontal flows where the non-orthogonal transformation causes large uncertainties in the vertical velocity (i.e., advancing our knowledge beyond the plausible scenario in Fig. 12f). It might also be possible to improve the calibration of the transducer measurements and thus reduce the uncertainty and potential underestimates of the vertical velocity for near-horizontal flows.

5 Conclusion

We conducted a manipulation experiment at the GLEES field site with an orthogonal anemometer (ATI 3Vx-probe) and used a Bayesian analysis to determine the most likely posterior 3D correction that allows vertically- and horizontally-mounted anemometers to yield similar measurements. In each experiment, the non-vertical mountings were used for testing and not intended for typical field deployments. Without applying the manufacturer-recommended transducer-shadowing correction there was a $\approx 10\%$ underestimate in the horizontal wind velocity components; when that correction was applied, the bias between the horizontal and vertical dimensions was mitigated (i.e., there were non-significant changes in the standard deviations of horizontal velocity components and in the horizontal temperature covariance). The latter result was robust with assumptions about the most accurate measurement of this anemometer. We conducted two manipulation experiments with a non-orthogonal anemometer (Gill R3-50) and used a Bayesian analysis to determine the most likely posterior 3D correction that allows anemometers mounted vertically, horizontally, and tilted by 45° to yield similar measurements. In an experiment at the GLEES field site, the posterior correction caused a 13–18% increase in the standard deviation of vertical velocity, which corresponded to a 6–10% increase in the covariance $\overline{w'T'}$, which is directly related to sensible heat flux or buoyancy flux. These values are similar to the discrepancies of 13% in the standard deviation of vertical velocity and 8% in sensible heat flux between the Gill R3-50 and ATI 3Vx-probe observed during the AmeriFlux site visit that motivated this study. These results rely on an assumption that the horizontal velocity measurements are most accurate with this anemometer, which, based on the manufacturer's calibration routine, we believe is justified. Results from a replicated experiment at the Pawnee National Grassland were inconclusive, probably due to the limited range of angle of attack. We demonstrated that a mathematical consequence of the non-orthogonal geometry is that errors in the vertical velocity measurements are unpredictable and can be enhanced for near-horizontal angles of attack. Due to this, it is plausible that that vertical velocity errors with a magnitude > 5% could exist for angles of attack within $\pm$ 14° for non-orthogonal anemometers with transducers tilted $\pm$ 45° from horizontal. Considering a similar study found the CSAT3 underestimated the standard deviation of vertical velocity by 8–14%, which corresponded to a 7–13% underestimate in sensible heat flux (Frank et al. 2016a), this methodology has indicated that multiple non-orthogonal anemometer designs could underestimate vertical velocity. Because of the mathematical consequences of the non-orthogonal transformation, we conclude that a mechanism exists that can lead to systematic biases in vertical velocity for all non-orthogonal anemometers with transducers tilted $\pm$ 45° from horizontal, making it plausible that many commonly used non-orthogonal anemometers could experience similar errors. This would have major implications for almost all eddy covariance–based studies of energy and trace gas exchange between the land surface and atmosphere.

Acknowledgements We thank Rickard McKay and Gill Instruments, Ltd. for providing details about the R3-50 calibration procedure, Jared Baker for assistance with the Mount Moran high-performance computer, Shannon Kay for advice with parallel Bayesian analysis, three anonymous reviewers for their thoughtful comments on the manuscript, and John Korfmacher for his help deploying the experiment in February at the GLEES field site during remarkably bad weather. Finally, we sincerely thank the late Henry Gholz who helped us remove instrumentation from the GLEES scaffolding on an equally terrifying day in March. This study was funded by the USDA Forest Service, the AmeriFlux Management Project, which is supported by the Office of Biological and Environmental Research in the U.S. DOE Office of Science as part of Terrestrial Ecosystem Science Program under the Contract DE-AC0205CH11231 to the Lawrence Berkeley National Laboratory, and Southwest Research Institute.

Appendix: Non-orthogonal Vertical Velocity Measurements are Unpredictable for Near-Horizontal Angles of Attack

If any systematic measurement errors occur with non-orthogonal sonic anemometer transducers, then the vertical wind velocity will have an unpredictable measurement error, or conversely an unpredictable correction, for near-horizontal flows. While transducer shadowing is a well-documented source of systematic measurement error (Kaimal 1979), this is generalizable for any cause of bias. The following derivation is an adaptation from the open-access discussion of Mauder and Zeeman (2018) (https://www.atmos-meas-tech.net/11/249/

2018/amt-11-249-2018-discussion.html) and applies to non-orthogonal anemometers with transducers tilted 45° from the horizontal plane, including the Gill R3-50. Assuming systematic transducer measurement errors can be corrected with a set of arbitrary functions α, the corrected vertical wind component in sonic coordinates, $\hat{w}_s$, is evaluated by substituting the corrected transducer velocities $u_1\alpha_1$, $u_2\alpha_2$, and $u_3\alpha_3$ into Eq. 1

$$\hat{w}_s = \frac{\sqrt{2}}{3}[u_1\alpha_1(\lambda, \varphi) + u_2\alpha_2(\lambda, \varphi) + u_3\alpha_3(\lambda, \varphi)]. \tag{6}$$

This can be expressed as a relative correction by dividing by the uncorrected w_s

$$\frac{\hat{w}_s}{w_s} = \frac{\sqrt{2}}{3}\left[\frac{u_1}{w_s}\alpha_1(\lambda, \varphi) + \frac{u_2}{w_s}\alpha_2(\lambda, \varphi) + \frac{u_3}{w_s}\alpha_3(\lambda, \varphi)\right]. \tag{7}$$

The relative correction can be expressed using only sonic coordinates by substituting with Eq. 2,

$$\frac{\hat{w}_s}{w_s} = \frac{\sqrt{2}}{3}\left[\frac{\frac{\sqrt{3}}{2\sqrt{2}}u_s + \frac{1}{2\sqrt{2}}v_s + \frac{1}{\sqrt{2}}w_s}{w_s}\alpha_1(\lambda, \varphi) + \frac{-\frac{1}{\sqrt{2}}v_s + \frac{1}{\sqrt{2}}w_s}{w_s}\alpha_2(\lambda, \varphi) + \frac{-\frac{\sqrt{3}}{2\sqrt{2}}u_s + \frac{1}{2\sqrt{2}}v_s + \frac{1}{\sqrt{2}}w_s}{w_s}\alpha_3(\lambda, \varphi)\right], \tag{8}$$

which can be further simplified as

$$\frac{\hat{w}_s}{w_s} = \frac{1}{3}\left[\left(\frac{\sqrt{3}}{2}\frac{u_s}{w_s} + \frac{1}{2}\frac{v_s}{w_s} + 1\right)\alpha_1(\lambda, \varphi) + \left(-\frac{v_s}{w_s} + 1\right)\alpha_2(\lambda, \varphi) + \left(-\frac{\sqrt{3}}{2}\frac{u_s}{w_s} + \frac{1}{2}\frac{v_s}{w_s} + 1\right)\alpha_3(\lambda, \varphi)\right]. \tag{9}$$

By definition, $\tan(\lambda) = v_s/u_s$ and $\tan(\varphi) = w_s/\sqrt{u_s^2 + v_s^2}$, such that the ratios u_s/w_s and v_s/w_s can be expressed as

$$\frac{u_s}{w_s} = \frac{\cos\lambda}{\tan\varphi} \tag{10}$$

and

$$\frac{v_s}{w_s} = \frac{\sin\lambda}{\tan\varphi}. \tag{11}$$

Equations 10 and 11 can be substituted into Eq. 9

$$\frac{\hat{w}_s}{w_s} = \frac{1}{3}\left[\left(\frac{\sqrt{3}}{2}\frac{\cos\lambda}{\tan\varphi} + \frac{1}{2}\frac{\sin\lambda}{\tan\varphi} + 1\right)\alpha_1(\lambda, \varphi) + \left(-\frac{\sin\lambda}{\tan\varphi} + 1\right)\alpha_2(\lambda, \varphi) + \left(-\frac{\sqrt{3}}{2}\frac{\cos\lambda}{\tan\varphi} + \frac{1}{2}\frac{\sin\lambda}{\tan\varphi} + 1\right)\alpha_3(\lambda, \varphi)\right]. \tag{12}$$

It is important to distinguish that λ and φ are the original/uncorrected wind direction and angle of attack based on original/uncorrected transducer measurements. An equation similar to Eq. 12 can be expressed with respect to the corrected angles $\hat{\lambda}$ and $\hat{\varphi}$,

$$\frac{w_s}{\hat{w}_s} = \frac{1}{3}\left[\left(\frac{\sqrt{3}}{2}\frac{\cos\hat{\lambda}}{\tan\hat{\varphi}} + \frac{1}{2}\frac{\sin\hat{\lambda}}{\tan\hat{\varphi}} + 1\right)\alpha_1\left(\hat{\lambda}, \hat{\varphi}\right) + \left(-\frac{\sin\hat{\lambda}}{\tan\hat{\varphi}} + 1\right)\alpha_2\left(\hat{\lambda}, \hat{\varphi}\right) + \left(-\frac{\sqrt{3}}{2}\frac{\cos\hat{\lambda}}{\tan\hat{\varphi}} + \frac{1}{2}\frac{\sin\hat{\lambda}}{\tan\hat{\varphi}} + 1\right)\alpha_3\left(\hat{\lambda}, \hat{\varphi}\right)\right]. \tag{13}$$

In Eq. 12, the left-hand side is the relative correction while in Eq. 13 it is the relative error. Finally, the limit of the relative correction as the angle of attack becomes near-horizontal is

$$\lim_{\varphi\to 0}\frac{\hat{w}_s}{w_s} = \frac{1}{3}\left(\alpha_1(\lambda,\varphi)+\alpha_2(\lambda,\varphi)+\alpha_3(\lambda,\varphi)\right) + \frac{1}{3}\left[\left(\frac{\sqrt{3}}{2}\cos\lambda+\frac{1}{2}\sin\lambda\right)\alpha_1(\lambda,\varphi)+(-\sin\lambda)\alpha_2(\lambda,\varphi)+\left(-\frac{\sqrt{3}}{2}\cos\lambda+\frac{1}{2}\sin\lambda\right)\alpha_3(\lambda,\varphi)\right]\lim_{\varphi\to 0}\frac{1}{\tan\varphi}, \quad (14)$$

which approaches $\pm\infty$ for most α functions and leads directly to Eq. 5.

References

Advanced Research Computing Center (2012) Mount Moran: IBM System X cluster. University of Wyoming, Laramie

Billesbach DP, Chan SW, Cook DR, Papale D, Bracho-Garrillo R, Verfallie J, Vargas R, Biraud SC (2019) Effects of the Gill-Solent WindMaster-Pro "w-boost" firmware bug on eddy covariance fluxes and some simple recovery strategies. Agric For Meteorol 265:145–151

Burns S, Horst T, Jacobsen L, Blanken P, Monson R (2012) Using sonic anemometer temperature to measure sensible heat flux in strong winds. Atmos Meas Tech 5:2095–2111

Frank JM, Massman WJ, Ewers BE (2013) Underestimates of sensible heat flux due to vertical velocity measurement errors in non-orthogonal sonic anemometers. Agric For Meteorol 171–172:72–81

Frank JM, Massman WJ, Ewers BE, Huckaby LS, Negrón JF (2014) Ecosystem CO_2/H_2O fluxes are explained by hydraulically limited gas exchange during tree mortality from spruce bark beetles. J Geophys Res Biogeosci 119:1195–1215

Frank JM, Massman WJ, Ewers BE (2016a) A Bayesian model to correct underestimated 3-D wind speeds from sonic anemometers increases turbulent components of the surface energy balance. Atmos Meas Tech 9:5933–5953

Frank JM, Massman WJ, Swiatek E, Zimmerman HA, Ewers BE (2016b) All sonic anemometers need to correct for transducer and structural shadowing in their velocity measurements. J Atmos Ocean Technol 33:149–167

Friebel HC, Herrington TO, Benilov AY (2009) Evaluation of the flow distortion around the Campbell Scientific CSAT3 sonic anemometer relative to incident wind direction. J Atmos Ocean Technol 26:582–592

Geissbühler P, Siegwolf R, Eugster W (2000) Eddy covariance measurements on mountain slopes: the advantage of surface-normal sensor orientation over a vertical set-up. Boundary-Layer Meteorol 96:371–392

Ghaemi-Nasab M, Franchini S, Davari AR, Sorribes-Palmer F (2018) A procedure for calibrating the spinning ultrasonic wind sensors. Meas 114:365–371

Gill Instruments Limited (2005) Omnidirectional (R3-50) Ultrasonic anemometer user manual. Document Number: 1210-PS-0011 Issue 04, p 67

Gill Instruments Limited (2017) R3-50, R3-100 and R3A-100 user manual. Document Number: 1210-PS-0015 Issue 1, p 55

Grare L, Lenain L, Melville WK (2016) The Influence of wind direction on Campbell Scientific CSAT3 and Gill R3-50 sonic anemometer measurements. J Atmos Ocean Technol 33:2477–2497

Hawkins DM (2004) The problem of overfitting. J Chem Inf Comput Sci 44:1–12

Hobbs NT, Hooten MB (2015) Bayesian models: a statistical primer for ecologists. Princeton University Press, Princeton

Horst T, Semmer S, Maclean G (2015) Correction of a non-orthogonal, three-component sonic anemometer for flow distortion by transducer shadowing. Boundary-Layer Meteorol 155:371–395

Huq S, De Roo F, Foken T, Mauder M (2017) Evaluation of probe-induced flow distortion of Campbell CSAT3 sonic anemometers by numerical simulation. Boundary-Layer Meteorol 165:9–28

Kaimal JC (1979) Sonic anemometer measurement of atmospheric turbulence. In: Proceedings of the dynamic flow conference 1978 on dynamic measurements in unsteady flows, Skovlunde, Denmark: proceedings of the dynamic flow conference 1978, Skovlunde, Denmark, pp 551–565

Kaimal JC, Gaynor JE, Zimmerman HA, Zimmerman GA (1990) Minimizing flow distortion errors in a sonic anemometer. Boundary-Layer Meteorol 53:103–115

Kochendorfer J, Meyers TP, Frank JM, Massman WJ, Heuer MW (2012) How well can we measure the vertical wind speed? Implications for fluxes of energy and mass. Boundary-Layer Meteorol 145:383–398

Kochendorfer J, Meyers TP, Frank JM, Massman WJ, Heuer MW (2013) Reply to the comment by Mauder on "How well can we measure the vertical wind speed? Implications for fluxes of energy and mass". Boundary-Layer Meteorol 147:337–345

Kruschke J (2014) Doing Bayesian data analysis: a tutorial with R, JAGS, and Stan. Academic Press, Cambridge

Loescher HW, Ocheltree T, Tanner B, Swiatek E, Dano B, Wong J, Zimmerman G, Campbell J, Stock C, Jacobsen L, Shiga Y, Kollas J, Liburdy J, Law BE (2005) Comparison of temperature and wind statistics in contrasting environments among different sonic anemometer-thermometers. Agric For Meteorol 133:119–139

Lu D, Ye M, Hill MC (2012) Analysis of regression confidence intervals and Bayesian credible intervals for uncertainty quantification. Water Resour Res 48:W09521

Mauder M (2013) A comment on "How well can we measure the vertical wind speed? Implications for fluxes of energy and mass" by Kochendorfer et al. Boundary-Layer Meteorol 147:329–335

Mauder M, Zeeman MJ (2018) Field intercomparison of prevailing sonic anemometers. Atmos Meas Tech 11:249–263

Mauder M, Oncley SP, Vogt R, Weidinger T, Ribeiro L, Bernhofer C, Foken T, Kohsiek W, De Bruin HAR, Liu H (2007) The energy balance experiment EBEX-2000. Part II: intercomparison of eddy-covariance sensors and post-field data processing methods. Boundary-Layer Meteorol 123:29–54

Mauder M, Eggert M, Gutsmuths C, Oertel S, Wilhelm P, Voelksch I, Wanner L, Tambke J, Bogoev I (2019) Comparison of turbulence measurements by a CSAT3B sonic anemometer and a high-resolution bistatic Doppler lidar. Atmos Meas Tech Discuss. https://doi.org/10.5194/amt-2019-133 **in review**

Nakai T, Shimoyama K (2012) Ultrasonic anemometer angle of attack errors under turbulent conditions. Agric For Meteorol 162–163:14–26

Neiswanger W, Wang C, Xing EP (2014) Asymptotically exact, embarrassingly parallel MCMC. In: Proceedings of the thirtieth conference on uncertainty in artificial intelligence, Quebec City, Quebec, Canada. AUAI Press, pp 623–632

Peña A, Dellwik E, Mann J (2019) A method to assess the accuracy of sonic anemometer measurements. Atmos Meas Tech 12:237–252

Rosenthal JS (2000) Parallel computing and Monte Carlo algorithms. Far East J Theor Stat 4:207–236

R Core Team (2015) R: a language and environment for statistical computing. R Foundation for Statistical Computing, Vienna, Austria. URL https://www.R-project.org/

Vickers D, Mahrt L (1997) Quality control and flux sampling problems for tower and aircraft data. J Atmos Ocean Technol 14:512–526

Wilkinson DJ (2006) Parallel bayesian computation. In: Kontoghiorghes EJ (ed) Handbook of parallel computing and statistics. Chapman & Hall/CRC, Boca Raton, pp 481–512

Wyngaard JC, Zhang S-F (1985) Transducer-shadow effects on turbulence spectra measured by sonic anemometers. J Atmos Ocean Technol 2:548–558